A time- and space-resolved nuclear receptor atlas in mouse liver

Francesco Paolo Zummo, Alexandre Berthier, Céline Gheeraert, Manjula Vinod, Marie Bobowski-Gérard, Olivier Molendi-Coste, Laurent Pineau, Matthieu Jung, Loic Guille, Julie Chevalier-Dubois, et al.

A time- and space-resolved nuclear receptor atlas in mouse liver

Francesco Paolo Zummo[1], Alexandre Berthier[1], Céline Gheeraert[1], Manjula Vinod[1], Marie Bobowski-Gérard[1], Olivier Molendi-Coste[1,$], Laurent Pineau[1], Matthieu Jung[2], Loic Guille[1], Julie Dubois-Chevalier[1], David Dombrowicz[1], Bart Staels[1], Jérôme Eeckhoute[1], Philippe Lefebvre[1,*]

[1]Univ. Lille, Inserm, CHU Lille, Institut Pasteur de Lille, U1011-EGID, F-59000 Lille, France.

[2]Univ. Strasbourg, CNRS UMR 7104, INSERM U1258 - GenomEast Platform - IGBMC - Institut de Génétique et de Biologie Moléculaire et Cellulaire, F-67404 Illkirch, France.

[$] Present affiliation: Univ. Lille, CNRS, Inserm, CHU Lille, Institut Pasteur de Lille, US 41 - UAR 2014 - PLBS, F-59000 Lille, France

* To whom correspondence should be sent.

Philippe Lefebvre

Inserm UMR1011, Bldg J&K

Faculté de Médecine Henri Warembourg, Pôle Recherche

Blvd du Prof Leclerc

59000, Lille, France

philippe-claude.lefebvre@inserm.fr

Tel +33.3.20974220

Short title: Nuclear receptors in mouse liver cell types

Keywords: nuclear receptors, liver, cell types, zonation, circadian

Word count: 5760 (main text)

ABSTRACT

The functional versatility of the liver is paramount for organismal homeostasis. Adult liver functions are controlled by a tightly regulated transcription factor network including nuclear receptors (NRs), which orchestrate many aspects of hepatic physiology. NRs are transcription factors sensitive to extracellular cues such as hormones, lipids, xenobiotics etc. and are modulated by intracellular signaling pathways. While liver functional zonation and adaptability to fluctuating conditions rely on a sophisticated cellular architecture, a comprehensive knowledge of NR functions within liver cell populations is still lacking. As a step toward the accurate mapping of NR functions in liver, we characterized their levels of expression in whole liver from C57Bl6/J male mice as a function of time and diet. *Nr1d1* (*Rev-erba*), *Nr1d2* (*Rev-erbb*), Nr1c2 (*Pparb/d*) and Nr1f3 (*Rorg*) exhibited a robust cyclical expression in ad libitum-fed mice which was, like most cyclically expressed NRs, reinforced upon time-restricted feeding. In a few instances, cyclical expression was lost or gained as a function of the feeding regimen. NR isoform expression was explored in purified hepatocytes, cholangiocytes, Kupffer cells, hepatic stellate cells and liver sinusoidal cells. The expression of some NR isoforms, such as *Nr1h4* (*Fxra*) and *Nr1b1* (*Rara*) isoforms, was markedly restricted to a few cell types. Leveraging liver single cell RNAseq studies yielded a zonation pattern of NRs in hepatocytes, liver sinusoidal cells and stellate cells, establishing a link between NR subtissular localization and liver functional specialization. In summary, we provide here an up-to-date compendium of NR expression in mouse liver in space and time.

INTRODUCTION

The liver is central to metabolism by coping with qualitatively and quantitatively fluctuating dietary intakes and it stores, packages and reroutes metabolic intermediates to other tissues. The liver also exerts other crucial functions such as detoxification, bile acid synthesis, immune and inflammatory responses and hemostasis. This versatility relies on precisely timed and spatially orchestrated activities of several resident and nonresident cell types which communicate intensively to achieve organ and whole body homeostasis. Within the functional unit of the liver, the hepatic lobule, the above-mentioned biological processes take place into several resident, highly connected cell types [hepatocytes (HC), cholangiocytes (CH), liver sinusoidal endothelial cells (LSEC), stellate cells (HSC) and Kupffer cells (KC)] which are functionally specialized. An additional layer of sophistication is the functional zonation of liver functions, which adapts to the centripetal blood, nutrients and oxygen flow and centrifugal bile circulation (Nagy et al., 2020).

As sensors of the environment through their ability to bind hormones, metabolic intermediates or xenobiotics, nuclear receptors (NRs) are essential relays of metabolic and endocrine signals regulating transcriptional networks in hepatic cells (Soccio, 2020). NR structure allows them to act directly or indirectly as transcriptional regulators (Weikum et al., 2018) and to integrate cues from extracellularly activated signaling pathways (Berrabah et al., 2011). Decade-long research efforts have established that NRs act in a tissue-specific manner through multiple mechanisms ranging from intracellular ligand activation to transcriptional coregulator combinatorial assembly on DNA-bound NR. This notion of a specific activity as a function of the site of expression is likely to be extended to distinct cellular populations within a given tissue, but technical hurdles related to single-cell approaches have to be solved prior to get a full appreciation of NR activity in a specific cell type.

In this respect, the liver is an optimal model to unravel mechanistic aspects of NR actions in cellular subpopulations, as single-cell approaches have paved the way to building a functional atlas of the liver lobule. Based on a thorough knowledge of liver histology, these transcriptomic analysis have partially established the zonation profile of gene expression in mouse and human livers (Payen et al., 2021, Droin et al., 2021, Aizarani et al., 2019, Dobie et al., 2019, Ben-Moshe et al., 2019, Ben-Moshe and Itzkovitz, 2019). However, quantitative and qualitative assessments of NR expression in the liver are scarce (Li et al., 2013, Gonzalez-Sanchez et al., 2017) but needed to fully appreciate their functional diversity and to leverage this knowledge to define innovative therapeutic strategies. Indeed, NR functions have been mostly defined in a hepatocyte background but their expression territory is more diverse. For example, NUR77 encoded by the *Nr4a1* gene is known to modulate hepatic glucose and lipid metabolism (Pols et al., 2008, Pei et al., 2006)and liver regeneration (Hu et al., 2014), but is

substantially expressed in CHs, LSECs and KCs from C57Bl/6 mouse liver (Gonzalez-Sanchez et al., 2017, Li et al., 2013) in which its functions are poorly characterized. Similarly, the physiology of the glucocorticoid receptor (GR), has historically been heavily characterized for its role in metabolic regulations (Praestholm et al., 2020), but whose expression in all other liver resident cell types is far from negligible (Gonzalez-Sanchez et al., 2017, Li et al., 2013).

Here, we have leveraged our different transcriptomic studies on bulk and purified liver cells to provide a thorough view of NR isoforms expression in simultaneously isolated parenchymal and non-parenchymal cell populations. Zonation of NR expression was also compiled from published single cell RNAseq studies (Halpern et al., 2018, Bahar Halpern et al., 2017, Su et al., 2021, Dobie et al., 2019) to allow for a refined appreciation of possible physiological NR functions

MATERIAL AND METHODS

Animal experimentation.

All experiments were approved by the Comité d'Ethique en Expérimentation Animale du Nord-Pas de Calais CEEA75 in compliance with European Union regulations. To eliminate sex as a confounder, only male mice were used throughout this study. C57BL6/J wild-type male mice (12-17 weeks) were purchased from Charles River Laboratories and housed in a temperature-controlled environment (23-25°C) with a 12h/12h light-dark cycle, ZT0 being lights-on. Mice had either free access to water and to a standard chow diet [Safe Diet A04)("AdLib(itum)" conditions] or access to food was restricted to the active period for 2 weeks prior to euthanasia (12 hours from ZT12 to ZT24)["T(ime)-R(estricted) F(eeding) condition]. Liver samples were collected every 3 hours at ZT0, ZT3, ZT6, ZT9, ZT12, ZT15, ZT18 and ZT21 for ad libitum fed mice. Livers were collected every 4 hours at ZT0, ZT4, ZT8, ZT12, ZT16, and ZT20 for the time restricted feeding study.

Multistep isolation of mouse parenchymal and non-parenchymal liver cells.

This protocol was optimized to isolate simultaneously hepatocytes (HCs), Kupffer cells (KC), hepatic stellate cells (HSCs), liver sinusoidal cells (LSECs)and cholangiocytes (CHs) from a single liver to obtain sufficient amounts of cells for transcription studies. Livers were obtained at ZT3 from an ad libitum-fed mouse.

Cell isolation: Mice (C57Bl6/J male, 12-17-week-old, Charles River) were euthanized by cervical dislocation at ZT3 and liver was perfused through the vena cava. After a first perfusion with Wash buffer [25mM Hepes, pH7.4, 4mM EGTA in 1x Hanks' Balanced Salt solution (HBSS, Gibco-ThermoFisher #14170)] at 37°C until discoloration of the liver, a second perfusion (≈50mL) was performed with Dissociation buffer (25mM Hepes, pH7.4, 1mM $CaCl_2$ in 1xHBSS) supplemented with collagenase (type IV, Sigma #C5138)(100U/mL) at 37°C. The liver was then removed and dissociated in a Petri dish. The cell solution was filtered through a 70µm cell filter and centrifuged for 2 min at 50 x G to collect HCs. HC pellets were washed once in 45mL Wash buffer, centrifuged for 2 min at 50 x G and resuspended in FACS buffer [1x phosphate-buffered saline (PBS), pH 7.4, 0.5% bovine serum albumin] supplemented with RNAsin (1:1000, Promega, #N2511) for FACS purification. The HC supernatants from the first centrifugation were collected and spun again for 2 min. at 50 x G to remove remaining HCs from the NPC fraction. NPC cells were then resuspended in Dissociation buffer. Seventy-five % of this preparation (NPC75) was added to the non-digested liver (recovered from the initial 70 µm filtration), centrifuged for 5 min at 580 x G and incubated with collagenase (100 U/mL), and 0.5

mg/mL pronase (Sigma-Aldrich, #10165921001) and 10 µg/mL DNAseI (DNase I grade II, from bovine pancreas, Sigma-Aldrich, # 10104159001) for 20 min at 37°C. The remaining 25% (NPC25) was further digested with collagenase alone for 10 min at 37°C. Cellular preparations were filtered through a 70 µm filter and centrifuged for 5 min at 580 x G in Wash buffer at 37°C. Both NPC fractions are resuspended in 1x FACS buffer supplemented with RNAsin and kept on ice before cell labelling.

Cell labelling: All steps from now on were performed at 4°C in light-protected conditions. Cellular fractions were spun down and resuspended in 1 mL red blood cell lysis buffer (155mM NH_4Cl, 10mM $NaHCO_3$, 0.127mM EDTA, pH7.4) for 4 min before adding 1 ml PBS + 0.5% BSA to stop lysis. Two to $3x10^6$ cells were dispatched per tube, centrifuged (5 min, 600 x G, 4°C) and resuspended in 1x PBS, 0.5% Zombie Green (Biolegend, #BLE423112), 1:1000 RNAsin (Promega, #N2511,) for 10 min. After centrifugation, cells were suspended in mouse BD FcBlock (1:200, Blocking anti-CD16/32, Becton-Dickinson #BD 553142), incubated for 15 min on ice and the antibody mix (see below) added for 20 min. Cells were washed twice in 1x FACS buffer and sorted.

Cell sorting: Cells were sorted using a BD INFLUX v7 cell sorter (BDBiosciences) driven by the BD FACS Sortware. Compensation particles were from Becton-Dickinson (BD™ CompBeads Compensation Particles Anti-Rat/Hamster Ig, κ Set, # 51-90-9000949). Fluorochrome-coupled antibodies (BioLegend) targeted CD31-BV421 (#BLE102424), CD45-BV510 (#BLE103138), CD326-CF594 (#BLE118236) F4/80-PE-Cy7 (#BLE123114) CD146-APC (#BLE134712) MHCII-AF700-(#BLE107622) CD11b-APC-Cy7 (#BLE101226). Anti-CLEC4F was from R&D (#MAB2784) and coupled to CF568 using the Mix-n-Stain CF568 Antibody Labeling Kit (Biotium, #BTM92235). All antibodies were used at 1:100 dilution. HCs sorting was performed using a 200 µm nozzle and the following settings: pressure 3.7 psi, drop frequency 6.30 kHz, piezo amplitude 4.1, sample fluid pressure was adapted to reach a maximum events rate of 1 000 events/sec. HCs were selected as viable large cells as visualized on FSC/SSC dotplot, and subsequently gated on singlets before sorting (Supplementary Figure 1).

Non parenchymal cells were sorted as follows: the INFLUX cell sorter was equipped with a 86 µm nozzle and tuned at a pressure of 24.7 psi, a drop frequency of 48,25 kHz, a piezo amplitude of 6.7 and sample fluid pressure was adapted to reach a maximum events rate of 10 000 events/sec. NPCs fractions (both NPC75 and NPC25, Supplementary Figure 1B) were gated for viable singlet cells as visualized on FSC/SSC and FSC-W/FSC-A dotplots, respectively and live cells were then selected as "Zombie Green low" events. HSCs were selected as UV^+ granular cells out of the NPC75 fraction, taking advantage of UV light excitation of retinol and retinoic acid contained in HSCs granules (Mederacke et al., 2015). A "non-small HSCs" gating was applied in order to avoid sorting of degranulated or damaged HSCs. LSECs were selected as UV^- $CD45^-$ $CD146^{hi}$ events of the NPC25 fraction as pronase digestion was

not compatible with CD31 detection. CHs were selected as UV^- $CD45^-$ $CD146^{low}$ $CD326^+$ events of the NPC75 fraction. KCs were selected as UV^- $CD45^+$ $F4/80^+$ $CLEC4F^+$ events of the NPC75 fraction, and a "non-small KCs" gating was applied in order to avoid sorting of immature or damaged KCs.

Sorted viable HCs were collected in 1 mL RNAlater (ThermoFisher, # 10564445) while sorted viable NPCs were collected in lysis buffer and further processed for RNA extraction. Cytometry data were analyzed using FlowJo v10.5.3 (FlowJo, LLC).

Immunofluorescence on sorted liver cells.

Cell preparations were deposited on a glass slide using a Cytospin 4 (ThermoScientific). Cells were fixed in 4% paraformaldehyde for 10 min and washed twice in 1x Phosphate-Buffered Saline (PBS). After blocking with 10% normal goat serum in 1x Tris-buffered saline (TBS) for 1 hour at room temperature (RT), slides were incubated with the primary antibody for 1 hour at RT or overnight at 4°C. After 3 washes in 1x TBS, secondary antibodies were added at the indicated dilution in 1x TBS for 1 hour at RT. Slides were washed as above and prepared for microscopy.

Primary antibodies used were: Anti-KRT18 (C-04, Abcam, #ab668)(dilution 1:100), anti-DESMIN (Y66, Abcam, #ab32362)(dilution 1:50), anti-CLEC4F (ThermoFisher, # MA5-24113)(dilution 1:100), anti-VECAD (ThermoFisher, # 36-1900)(dilution 1:50), anti-KRT19 (EP1580Y, Abcam, # ab52625)(dilution 1:100). Secondary antibodies (ThermoFisher Scientific) were used at 1:100 dilution and were goat anti-mouse AF568 (A-11004), donkey anti-rabbit AF488 (A-21206), donkey anti-mouse AF555 (A-31570) and goat anti-rat AF488 (A-11006).

RNA extraction and RT-qPCR.

RNA was extracted using the Macherey-Nagel™ Mini kit Nucleospin™ (Macherey-Nagel, # 872061) or Qiagen RNeasy micro kit (Qiagen, # 74004), depending on abundance of cell preparations, following the manufacturer's instructions. RNA concentration and purity were assessed using a Nanodrop One device (ThermoFisher Scientific) or a Qubit fluorometer (ThermoFisher Scientific) and a Qubit RNA HS Assay kit (ThermoFisher Scientific, # Q32852), while RNA integrity was analyzed on a Bioanalyzer 2100 (Agilent). RNA preparations with RIN<6.0 were discarded. RNAs were reverse-transcribed using random primers and the High Capacity cDNA Reverse Transcription Kit (ThermoFisher/Applied Biosystems, # 4368814). Quantitative PCR was performed in technical triplicates from at least 3 independent biological samples using the SYBR green Brilliant II fast kit

(Agilent Technologies) on an Mx3005p apparatus (Agilent Technologies) or a QuantStudio 3 (Applied Biosystems). Expression values obtained from mRNA levels normalized to *Rps28* (ribosomal protein S28) and *Rplp0* (acidic ribosomal phosphoprotein P0) mRNA levels and were used to calculate fold changes using the cycle threshold ($2^{-\Delta\Delta Ct}$) method (Schmittgen and Livak, 2008). Primer sequences are listed in Supplemental Table 1. PCR primer efficiencies were routinely assessed by serial 2-fold dilution of a control cDNA source (in the 1 to 500-fold range), the size of the amplicon was checked by agarose electrophoresis and the specificity of the PCR amplicon was systematically assessed by melting curve analysis. In this study, RT-qPCR results were always confirmed with RNAseq data.

Affymetrix array analysis.

RNA processing and array hybridization: Gene expression from whole mouse liver (n=3) was analyzed with Affymetrix GeneChip MoGene 2.0 ST arrays after RNA amplification, sscDNA labeling and purification. Briefly, RNA was amplified using the GeneChip™ WT PLUS Reagent Kit (Thermo Fisher Scientific, # 902280), retrotranscribed to single-stranded complementary (ssc) DNA and labeled using GeneChip™ WT Terminal Labeling Kit (Thermo Fisher Scientific, # 900670), followed by hybridization on the GeneChip Mouse Gene 2.0 ST Array (Affymetrix, # 902118) according to the manufacturer's instructions.

Data processing and analysis: Raw data were processed on a local instance of Galaxy (Afgan et al., 2018) using GIANT, a user-friendly tool suite developed in-house for microarray and RNA-seq differential data analysis (Vandel et al., 2020). It consists of modules allowing to perform quality control (QC), Robust Multiarray-Average method normalization, LIMMA differential analysis, volcano plot and heatmaps. Signals were normalized with GIANT APTtool (v2.10.0, ThermoFisher) with options "gc correction, scale intensity and rma at probeset level" followed by a $\log_2$ transformation. Then normalized expressions were averaged per Gene Symbol (NetAffx Annotation Release 36, July, 2016) and transcripts within the 10^{th} lowest percentile were considered as technically unreliable and excluded. Differential analysis was performed with GIANT limma tool [v3.36.5, (Ritchie et al., 2015)] (FDR cutoff = 0.05) "

RNA sequencing.

Library preparation and sequencing: RNA samples (n=3) were sent to the GenomEast platform for library preparation and sequencing. Briefly, RNA preparations were first depleted from unwanted, abundant transcripts using Ribo-Zero Plus rRNA depletion kit (Illumina, # 20040526). cDNA synthesis,

3'end adenylation, adapter ligation and PCR amplification were performed using the TruSeq Stranded total RNA sample preparation kit (Illumina). DNAs were sequenced using an Illumina HiSeq 4000 sequencer in 50 bp Single-Read following Illumina's instructions. Image analysis and base calling were performed using RTA 2.7.7 and bcl2fastq 2.17.1.14. Sequencing depth was 75 million reads on average.

Data processing and analysis: Reads were preprocessed using cutadapt version 1.10 (Kechin et al., 2017) in order to remove adapter, polyA and low-quality sequences (Phred quality score below 20). Reads shorter than 40 bases were discarded for further analysis. Remaining reads were mapped onto the mm10 assembly of the Mus *musculus* genome using STAR version 2.5.3a (Dobin et al., 2013). Gene expression quantification was performed from uniquely aligned reads using htseq-count version 0.6.1p1 (Anders et al., 2015), with annotations from Ensembl version 94 and "union" mode. Read counts were normalized across samples with the median-of-ratios method (Anders and Huber, 2010), suitable for inter-sample comparison. Gene expression profiles were compared using the Bioconductor package DESeq2 version 1.16.1 (Love et al., 2014). P-values were adjusted for multiple testing using the Benjamini and Hochberg method (Benjamini and Hochberg, 1995).

Splice junctions and isoform detection: Splice junctions were visualized in Integrative Genomics Viewer (IGV, Broad Institute)(Robinson et al., 2011) using bam files of aligned reads and the mm10 gene annotation track. Alignment data were visualized using the Sashimi plot function of IGV.

Single cell data extraction.

Analysis were carried out using extracted data from available datasets (GSE84490 for HC zonation and GSE108561 for LSEC zonation) obtained from 6 to 16-week-old C57BL/6 male mice (Halpern et al., 2018, Bahar Halpern et al., 2017). We used the ISCEBERG browser which allows analysis and interrogation of single cell RNAseq data (Guille et al., 2022) for HSC zonation [GSE137720 (Dobie et al., 2019)] and LSEC zonation [GSE147581, (Su et al., 2021)].

HSCs, GSE137720: Seurat (v 4.0.1) was used to analyze this dataset. Cells were obtained from *Pdgfrb*-BAC-eGFP reporter mice on a C57BL/6 background (10 to 16-week-old males). According to (Dobie et al., 2019), we filtered out cells expressing < 300 genes and cells expressing > 30 % of mitochondrial genes. Then data were normalized and scaled using NormalizeData (normalization.method=LogNormalize, scale.factor=10000) and ScaleData (features=all.genes) functions from the Seurat package. We applied a batch correction using Harmony (v 0.1.0). Then dimensionality reduction was achieved using Uniform Manifold Approximation and Projection (UMAP) to calculate 2D coordinates (reduction="harmony",dims=1:30). SCINA (v 1.2.0) was used to characterize cell populations (fibroblasts, vascular smooth muscle cells, and hepatic stellate cells) according to cell

markers defined in (Dobie et al., 2019). Cells distinct from HSCs were filtered out and HSCs located in the periportal or pericentral areas were identified using SCINA (version 1.2.0) based on markers used in the publication.

LSECs, GSE147581: Seurat (v 4.0.1) was used to analyze this dataset. Cells were obtained from Cdh5-CreERT2, mT/mG mice of undefined sex. According to (Su et al., 2021), cells expressing less than 200 transcripts and more than 20 % of mitochondrial genes were filtered out. Data were normalized and scaled as above, and Harmony (version 0.1.0) was used to apply a batch correction. UMAP coordinates were calculated and clusterized with findClusters using a resolution of 0.5 to match with the published analysis. Annotation with identified zonation markers was carried out using SCINA (version 1.2.0).

Statistical analysis.

Statistical analysis was performed using GraphPad Prism (v. 9). Data are plotted as the mean ± SEM. At least 3 independent experimental replicates were obtained. Data were determined to have equal variances using the F test. For 2-group comparisons, an unpaired 2-tailed *t*-test with Welch correction was used. For multiple comparisons with one variable, a 1-way ANOVA followed by the Tukey multiple comparison test (each group compared to every other group) was used. Multiple comparisons with more than one variable were carried out using a 2-way ANOVA followed by a Tukey's multiple comparison test. Cyclical patterns of gene expression were determined using JTK_Cycle (version 3.1)(Hughes et al., 2010). Cyclic circadian transcripts were defined as such when having a period between 21-26 hours and an adjusted p-value <0.05. All samples were incorporated in the analysis (Ad libitum-fed: ZT0, ZT3, ZT6, ZT9, ZT12, ZT15, ZT18 and ZT21; TRF: ZT0, ZT4, ZT8, ZT12, ZT16, and ZT20).

Data visualization.

Bubbleplots: Bubbleplots were generated in R studio using the ggplot2, plotly, reshape2, rcpp and tidyverse packages. SVG files were modified with Inkscape v1.0 and assembled as figures using CorelDraw2020. The liver trabeculae structure was adapted from a file published in a Public Library of Science journal (Frevert et al., 2005) under the Creative Commons Attribution 4.0 license.

Data availability.

Affymetrix data files ("AdLib" and "TRF" data) are available under NCBI GEO (https://www.ncbi.nlm.nih.gov/geo/) dataset numbers GSE223360 and GSE224446 respectively. RNA sequencing data are available under the GEO dataset number GSE222597.

RESULTS

Development of a liver cell type multi-step isolation protocol.

In order to minimize both technical and biological biases in isolating liver cell populations, we set up a protocol allowing the purification of 5 resident cell populations, i.e. HCs, LSECs, HSCs, KCs and CHs from a single liver. This protocol also allowed the purification of dendritic cells and of neutrophils, which were not considered further in this study. After sacrifice by cervical dislocation to avoid any side effects of anesthetics, the liver was perfused with modified HBSS and dissociated with collagenase IV. To enrich for specific cell populations, aliquots of the digested liver were then processed separately (Figure 1). Dissociated cells were sorted based on size to yield purified HCs, whose amounts routinely exceeded 20 x10^6 cells per liver. Further digestion by collagenase and pronase yielded the total non-parenchymal cell (NPC) fraction which was sorted using the indicated combination of antibodies (Figure 1 and Supplemental Figure 1). This yielded per liver variable amounts of HSCs, KCs, LSECs and CHs with numbers routinely exceeding 10^5 cells per preparation and cell type (Supplemental Figure 2). Cellular homogeneity and purity were assessed by RT-qPCR and immunofluorescence using established cell type-specific cellular markers (Figures 2 and supplemental Figure 3).

Circadian rhythmicity of hepatic nuclear receptors expression.

In homeostatic conditions, NR expression may vary not only as a function of nutritional and hormonal cues, but also according to the day-night cycle. To assess whether time-of-the-day is a critical parameter in dictating NR-encoding transcript abundance, we compared gene expression patterns in C57Bl6 male mice liver fed a chow diet either *ad libitum* or under time-restricted feeding for 10 days. In the latter case, food was available only during the active period (dark period for 12 hours, ZT12 to ZT24), while all other parameters were similar [number of mice per cage (4), temperature (22-24°C), access to water)]. Transcriptomic data were obtained and analyzed using the JTK package to determine gene expression periodicity (Hughes et al., 2010)(Supplemental Table 2). Several NRs displayed in ad libitum conditions a robust 23 to 24-hours cycle [*Nr1d1*(*Rev-erba*), *Nr1d2*(*Rev-erbb*), *Nr1c2*(*Pparb/d*) and *Nr1f3*(*Rorg*)] while *Nr2f6*(*Ear2*), *Nr2b1*(*Rxra*), *Nr1c1*(*Ppara*), *Nr2c2*(*Tr4*), *Nr1h4*(*Fxra*) and *Nr2a1*(*Hnf4a*) cycled similarly albeit with a lesser amplitude (Figure 3). With the exception of *Nr2a1*(*Hnf4a*), the time-restricted feeding regimen did not modify the cyclic expression pattern of these NRs (Figure 3 and Supplemental Table 2), while showing a trend to increase the amplitude of the signal. More surprisingly, several NRs exhibited condition-specific cycling [ad

libitum-fed: *Nr4a2*(*Nurr1*), *Nr5a2*(*Lrh1*), *Nr1f1*(*Rora*), *Nr3c2*(*Mr*), *Nr1i2*(*Pxr*), *Nr1c3*(*Pparg*); time-restricted feeding: *Nr2b3*(*Rxrg*), *Nr1h2*(*Lxrb*), *Nr3c1*(*Gr*), *Nr1h3*(*Lxra*), *Nr2b2*(*Rxrb*), *Nr1i3*(*Car*)]. Irrespective of the functional consequences of such oscillations, these differential expression levels should be considered when comparing expression levels of NRs in different conditions. We thus selected ZT3 (3 hours after light-on) as a convenient reference time point to initiate liver cell type isolation from ad-libitum fed mice (Figure 1). In these conditions, *Nr1d1*(*Rev-erba*) and *Nr1d2*(*Rev-erbb*) reached their zenith, while *Nr1f3*(*Rorg*), *Nr1c3*(*Pparg*) and *Nr1i2*(*Pxr*) were at their nadir.

Nuclear receptor expression in liver cell types.

NR-encoding transcripts were quantified in each cell type by RNAseq (Figure 4 and Supplemental Table 3). Forty-two NRs reached a detectable level of expression (RPKM>10), and each cell type was characterized by a specific NR pattern of expression, with a high level in *Nr2a1*(*Hnf4a*), *Nr2f6*(*Ear2*), *Nr1c1*(*Ppara*) and *Car*(*Nr1i3*) mRNAs being characteristic of hepatocytes. Cholangiocytes exhibited a highly restricted panel of highly expressed NRs, including only *Nr1f1*(*Rora*) and *Nr2a2*(*Hnf4g*). LSECs showed high levels in *Nr1b2* and *b3* (*Rarb* and *g*), *Nr2f1* and *f2* (*Coup-tf1&2*), while HSCs were characterized by a high level in *Nr1h4* and *h5*(*Fxra* and *b*), *Nr1a1*(*Thra*) and *Nr1b1*(*Rara*). Finally, *Nr2b2*(*Rxrb*), *Nr4a1*(*Nur77*), *Nr1c3*(*Pparg*) and *Nr1h3*(*Lxra*) elevated levels were a feature of KCs. On the opposite, hepatocytes were characterized by undetectable levels in *Nr4a3*(*Nor1*) and LSECs by the total absence of *Hnf4g*. NRs deemed to be undetectable in any cell type (<10 RPKM) were *Erb*(*Nr3a2*), *Dax1*(*Nr0b1*), *Tlx*(*Nr2e1*), *Pnr*(*Nr2e3*), *Sf1*(*Nr5a1*), *Rorb*(*Nr1f2*) and *Pr*(*Nr3c3*).

Nuclear receptor isoforms expression in liver cell types.

Nuclear receptor isoforms play substantially distinct physiological roles, hence determining their expression level is of importance to decipher NR cell-specific functions. NR protein isotypes and their corresponding isoforms were compiled from Uniprot and Protein Ontology databases (UniProt, 2021, Natale et al., 2017), and associated transcripts were searched in RNAseq data using the Sashimi plot function from the Integrative Genome Viewer [IGV, (Katz et al., 2015, Robinson et al., 2011)]. Twenty out of the 42 detected NRs-encoding transcripts can be potentially expressed as distinct isoforms (Figure 5 and Supplemental Table 3) out of which 11 actually displayed differential expression in the 5 isolated liver cell types. These included transcripts coding for FXRα, PXR, CAR, GCNF, PPARγ,

RARα, β and γ, RORα, RXRβ, T3Rα and β, whose expression levels were qualitatively assessed as described and were reported in Figure 5.

Zonation of nuclear receptor expression in hepatocytes, sinusoidal endothelial cells and stellate cells.

Functional zonation of the liver is observed along a periportal-pericentral axis and is conditioned by multiple factors such as oxygen, nutrient and morphogen gradients (Panday et al., 2022, Kietzmann, 2017). Specialized functions of liver cell types as a function of their spatial distribution can be inferred from single-cell studies and have been molecularly detailed in recent years. Expression patterns of NR-encoding genes were extracted from published datasets for mouse HCs, LSECs and HSCs (Halpern et al., 2018, Bahar Halpern et al., 2017, Dobie et al., 2019, Su et al., 2021). In HCs, NRs displayed distinct spatial expression patterns)(Figure 6), with PPARα being equally expressed along the pericentral to periportal axis, in agreement with its ability to regulate fatty acid oxidation (predominantly periportal) and ketogenesis (predominantly pericentral). Other NRs also displayed an even gene expression pattern along this axis (Nr3c2(*Mr*), Nr1f1 and f3(*Rora* and *g*), *Nr6a1*(*Gcnf*), *Nr1a2*(*Thrb*), *Nr2f2*(*Coup-tf2*), *Nr0b2*(*Shp*), while some had a dominant pericentral localization [*Pparg(Nr1c3*), *Errb(Nr3b2*), *Nr5a2*(*Lrh1*), *Nr3c1*(*Gr*), *Nr2b2*(*Rxrb*). Only *Nr1d2*(*Rev-erbβ*) and *Era*(*Nr3a1*) were preferentially expressed in the portal area. Mining the transcriptome of LSECs obtained by paired-cell RNAseq (Halpern et al., 2018) defined NR expression in this cell population (Supplemental Figure 4). Thirty-seven NRs were found to have a spatially differential expression, with *Nr2c1*(*Tr2*), *Nr5a2*(*Lrh1*) and *Nr1c3*(*Pparg*) being almost exclusively expressed in the pericentral area. Mirroring this pattern, *Pxr*, *Era* and *Errg* were exclusively detected in the periportal area, while *Nr1f2*(*Coup-tf2*), *Nr1h2*(*Lxrb*), *Nr1c1*(*Ppara*), *Nr3c1*(*Gr*), *Nr1i3*(*Car*), *Nr2b1*(*Rxra*) and *Nr3b2*(*Esrrb*) were significantly expressed, albeit with variation, in all 4 layers. A comparison with CDH5 (VE-cadherin)-expressing LSEC single-cell transcriptome data brought further elements of comparison, while providing novel information about arterial (portal) and venous (central) LSECs (Supplemental Figure 5). Zonation patterns matched for 50% (18 out 37) NRs, showed minimal discrepancies for 15 and were strikingly different for *Nr1c1*(*Ppara*), *Nr3b1*(*Esrra*), *Nr3b3*(*Errg*) and *Nr3a1*(*Era*). *Nr1c1*(*Ppara*) expression levels, which are in LSECs 4% of that found in HCs, was restricted to arterial-like ECs (Supplemental Figure 5) or present all along the pericentral-periportal axis (Supplemental Figure 4). Along this axis, *Nr3a1*(*Era*), *Nr3b1*(*Esrra*) and *Nr3b3*(*Esrrg*) displayed an opposite gradient of expression in these 2 datasets. Mouse strains, sex as it is undefined in a study (Su et al., 2021), cell isolation and identification methods as well as transcript mapping procedures were different in those

2 studies, calling for additional strictly comparative studies to reach a consensual cartography of NRs in LSECs. Of note, our LSEC purification procedure relies on a CD31/CD146 double-positive labeling to obtain highly pure cell preparations, which may have nevertheless selected a particular subpopulation.

Finally, NR expression was mapped in the 2 identified HSC populations which locate in close vicinity to the periportal (PaHSCs) or of the pericentral (CaHSC) areas (Supplemental Figure 6). With the exception of *Fxra* whose expression was detected in both HSC subpopulations and slightly higher in PaHSCs, the 30 quantified NR-encoding transcripts showed a markedly unbalanced expression between the 2 subpopulations. *Nr2f2*(*Coup-tf2*), *Nr3c1*(*Gr*), *Nr2b1*(*Rxra*), *Nr1f1*(*Rora*), *Nr1h2*(*Lxrb*) and *Nr2f6*(*Ear2*) were more preferentially expressed on PaHSCs, whereas *Nr1a1*(*Thra*), *Nr4a1*(*Nur77*), *Nr1h5*(*Fxrb*), and *Nr1b1*(*Rara*) transcripts were prominently localized in CaHSCs.

DISCUSSION

Nuclear receptors play critical roles in liver physiology, and establishing a precise spatiotemporal atlas of their expression is mandatory to define their functions. A first study relying on PCR-based detection reported the tissue distribution pattern of human NRs, using a mixed source of RNAs (varying sex, age and ethnical origin, (Nishimura et al., 2004). A similar approach was applied to nonreproductive tissues isolated from male 129x1/SvJ and C57/Bl6J mice at ZT0 (Bookout et al., 2006). Both studies provided a first elegant assessment of the functional clustering of NRs on the basis of their tissue-specific expression. Recent progress in single-cell technologies has shed some light on processes driving liver functional zonation and allowed to map cell-specific expression patterns of NRs, but they still lack sensitivity to identify transcript isoforms in isolated cells. Here we provide a compendium of hepatic NR expression considering and minimizing whenever possible technical variability, diet and time-of-the-day influences. By performing a bulk RNAseq analysis of isolated cell types, NR transcript isoforms were also easily identified, as NR protein isoforms are known, at least for a few cases, to bear distinct functional properties. Finally, spatial expression of NRs has been explored by mining single cell transcriptomic datasets, which may provide a mean to ascribe, or rule out, novel functions to NRs.

Our data were compared with others, which were obtained from *ad libitum*-fed C57Bl/6J male (Gonzalez-Sanchez et al., 2017) or female mouse livers (Li et al., 2013) collected at non indicated times and using distinct cell isolation and RNA quantification methods. While methodologies and biological sources were different, these 3 sets of data identified unambiguously NRs which are never detected in any liver cell types [*Nr0b1*(*Dax1*), *Nr1f2*(*Rorβ*), *Nr2e1*(*Tlx*), *Nr3e3*(*Pr*) and *Sf1*(*Nr5a1*)]. Sexual dimorphism of NR gene expression was not addressed in the present study but has pathophysiological relevance (Della Torre and Maggi, 2017). *Nr1d1*(*Rev-erba*), *Nri3*(*Car*), *Nr1i2*(*Pxr*), *Nr1c1*(*Ppara*) indeed exhibit distinct circadian patterns when comparing C57BL/6 male and female mice (Lu et al., 2013).

Ad libitum or time-restricted access to a high fat diet showed that besides sexually dimorphic protective effects of TRF, it may also substitute to normal oscillations driven by the molecular clock (Chaix et al., 2021, Chaix et al., 2018, Vollmers et al., 2009). On an obesogenic diet, TRF tends to restore gene expression rhythmicity (Deota et al., 2023), which is blunted under a HFD when compared to a chow diet (Eckel-Mahan et al., 2013, Hatori et al., 2012). While our data concur to show a similar trend in our TRF experiment, some differences can be noted in other studies which can be ascribed to the duration of the regimen in a similar genetic background [10 days vs. 49 (Deota et al., 2023) or 100 days (Hatori et al., 2012)]. A sufficiently powered, strictly comparative study is required to draw formal

conclusions about the influence of the feeding regimen on the phase and amplitude of transcript oscillations.

Identifying an NR-based cell type signature requires to exclude NRs with oscillating levels of transcripts and strongly sensitive to feeding conditions. Since ad libitum feeding is most commonly used in animal facilities, we used this experimental condition as a reference and could identify *Rev-erba*(*Nr1d1*), *Rev-erbb*(*Nr1d2*), *Rorg*(*Nr1f3*), *Pxr*(*Nr1i2*) and *Car*(*Nr1i3*), *Fxra*(*Nr1h4*) and *Pparb/d*(*Nr1c2*) as genes with markedly oscillating transcripts along the day-night cycle. Of note, *Nr4a1*(*Nur77*)- and *Nr2c2*(*Tr4*)-encoded transcripts gained strong cyclicity in time-restricted fed mice. An NR consensus signature characteristic of HC could be defined which identified, when integrating isoform expression patterns. *Hnf4a1*, *Ppara* and *Thrb1* were overwhelmingly expressed in this cell type, with 10x expression ratios when compared to CHs, HSCs, LSECs or KCs. In CHs, *Rora2* and *Gcnf M2* isoforms expression were markedly higher than in other cell types (x5 to x10). In LSECs, both *Nr1f2*(*Coup-tf2*) and *Rarg2* displayed highest levels of expression, while *Era* and *Fxra1* and *a2* expression were hallmarks of HSCs. Finally, KCs displayed highest levels in *Nr3b1*(*Esrra*), *Nr1h3*(*Lxra*) and *Nr4a1*(*Nur77*). Our data thus bring additional information about NR isoform expression, which are in most cases in good agreement with previous reports for NRs displaying high to moderate expression levels. Some minor discrepancies were observed for NRs displaying low expression levels, which are reported as not expressed in PCR-based investigations, but nevertheless detected in the more sensitive RNAseq assay.

The zonated expression of NRs calls for a more detailed consideration of NR functions deduced from previous "bulk" approaches. We previously detailed the implication of the zonated expression of PPARs in HCs (Berthier et al., 2021). PPARα appears to be preferentially pericentral, together with PPARα-driven lipogenic enzymes. However, fatty acid oxidation, which is also controlled by PPARα, mostly occurs in the oxygen-rich periportal area where a decreased, but not absent, expression of *Pparα* is observed. In contrast, *Pparγ* is uniquely expressed in pericentral HCs, in line with its pro-lipogenic activities and the metabolic zonation of HCs. We note that *Rxrβ* is also preferentially expressed in the pericentral area. As a PPARγ heterodimerization partner, RXRβ confers increased transcriptional activity to PPARγ when compared to RXRα (Lefebvre et al., 2010). Although this remains to be formally proven, this raises the possibility of cell type-specific heterodimeric combinations with distinct transcriptional properties. Also consistent with the metabolic zonation of the liver, *Nr4a1* (*Nur77*) is mostly expressed in the periportal area where it may exert its pro-gluconeogenic activities (Pei et al., 2006). Finally, targeting a given NR in liver disease should integrate this spatial parameter. NASH-induced fibrosis stems mostly from a pericentral injury, likely to activate stellate cells in this

area. We note that NR agonists efficiently blocking NASH and fibrosis progression, at least in rodent models, display a preferential expression in central HSC (caHSC, Supplemental Figure 6).

Nineteen NRs detected in our study have referenced protein isoforms, a number likely to be vastly underestimated (Annalora et al., 2020). Therefore splicing events could dramatically extend the functional repertoire of NRs, as described for "metabolic NRs" (Mukha et al., 2021). While our study was not designed to formally quantify all alternative transcripts for each NRs expressed in each liver cell type, 13 NR-encoding genes were actually expressed as different isoforms. They included *Nr1h4*(*Fxra*), *Nr1h5*(*Fxrb*), *Nr1i2*(*Pxr*), *Nr1i3*(*Car*), *Nr6a1*(*Gcnf*), *Nr1c3*(*Pparg*), *Nr1b1, 2, 3*(*Rara*, *b* and *g*, *Nr1f1*(*Rora*), *Nr2b2*(*Rxrb*, Nr1a2) and *Nr1a3*(*T3ra* and *b*). Various *scenarii* were observed with respect to isoform expression profiles. A single isoform could be detected per cell type (*Nr1i2*, *Pxr*) or a single or a mix of isoforms were identified [*Nr1h4*(*Fxra*), *Nr1h5*(*Fxrb*), *Nr1i3*(*Car*), *Nr6a1*(*Gcnf*), *Nr3c3*(*Pparg*), *Nr1b1*(*Rara*), *Nr1b2*(*Rarb*), *Nr1b3*(*Rarg*), *Nr1f1*(*Rora*), *Nr2b2*(*Rxrb*)]. In most cases, isoform expression is known to result from alternative promoter usage (*Fxra1*, *a2* vs *Fxra3*, *a4*; *Pparg1* vs *Pparg2*; *Rara1* vs *Rara2*; *Rarg1* vs *RARg2*; *Rxrb1* vs *Rxrb2*) and in the remaining cases (*Rarb2* vs *Rarb4* and *Rora1* vs *Rora2*) from alternative splicing. While the specific functions of NR isoforms has not been studied in great details with a few exceptions (FXR, PPARγ), reports generally point at distinct transcriptional activities and tissue-specific expression of these variants (Mukha et al., 2021). This knowledge has to be refined by investigating the role of NR isoforms in liver cell subpopulations, which exert distinct roles that still remain to be explored. In this respect, the subtissular repartition of FXR, which in contrast to 2 reports (Verbeke et al., 2014, Fickert et al., 2009), we and others (Gonzalez-Sanchez et al., 2017, Garrido et al., 2021) found to be highest expressed in HSCs and less abundantly in HCs, should be refined in light of isoform expression territories. FXR isoform functions have indeed been studied by elegant approaches solely in a hepatocyte background, in which FXRα1 and α2 were described to differentially affect bile acid and lipid metabolism (Vaquero et al., 2013, Ramos Pittol et al., 2020, Correia et al., 2015, Boesjes et al., 2014). We observed that HCs mostly express FXRα3 and α4, whereas HSCs express mostly FXRα1 and α2. This calls for a careful reexamination of FXR isoforms' biological properties in each cell (sub)type such as CaHSCs and PaHSCs, which is currently underway in our laboratory.

Taken as a whole, this study provides a compendium of NR expression in parenchymal and non-parenchymal liver cells which calls for an in-depth investigation of NR functions in liver cell populations. In addition to the multiple layers of NR activity regulation, that ranges from ligand availability, dimerization, transcriptional comodulator interaction and post-translational modifications, the expression territory, hence the cellular background is likely to confer specific

properties to NR-controlled signaling pathways, and this mapping will provide new guidance for NR-based therapies.

FUNDING

This work and FPZ were supported by an advanced ERC grant (to BS, Immunobile #694717), by the ANR-funded "European Genomic Institute for Diabetes" E.G.I.D. (ANR-10-LABX-0046), a French State fund under the frame program Investissements d'Avenir I-SITE ULNE/ANR-16-IDEX-0004 ULNE, and by a grant from Fondation pour la Recherche Médicale (Equipe FRM EQU202203014645 to PL). The authors are indebted with the GenomEast sequencing platform for continuous support and advices.

DECLARATIONS of INTEREST

The authors have nothing to declare.

AUTHOR's CONTRIBUTIONS

Author's contributions were: Conceptualization: FPZ, BS, PL; Methodology: FPZ, AB, MV, OMC, LG, CG, DD, MBG, LP; Software: LG, JCD, MJ; Validation: FPZ, OMC, JCD, CG, MJ, LP; Formal analysis: FPZ, AB, MBG, PL; Investigation: FZ, AB, OMC, LP, CG, MBG; Resources: DD, PL, BS; Data Curation: FPZ, LG, JE, PL; Writing: DD, FPZ, PL; Visualization: FPZ, OMC, PL; Supervision: PL, JE, JCD, DD, BS; Project administration: PL, DD, BS; Funding acquisition: PL, DD, BS

REFERENCES

Afgan, E., Baker, D., Batut, B., Van Den Beek, M., Bouvier, D., Cech, M., Chilton, J., Clements, D., Coraor, N., Grüning, B. A., Guerler, A., Hillman-Jackson, J., Hiltemann, S., Jalili, V., Rasche, H., Soranzo, N., Goecks, J., Taylor, J., Nekrutenko, A. & Blankenberg, D. 2018. The Galaxy platform for accessible, reproducible and collaborative biomedical analyses: 2018 update. *Nucleic Acids Res,* 46**,** W537-w544. https://doi.org/10.1093/nar/gky379

Aizarani, N., Saviano, A., Sagar, Mailly, L., Durand, S., Herman, J. S., Pessaux, P., Baumert, T. F. & Grun, D. 2019. A human liver cell atlas reveals heterogeneity and epithelial progenitors. *Nature*. https://doi.org/10.1038/s41586-019-1373-2

Anders, S. & Huber, W. 2010. Differential expression analysis for sequence count data. *Genome Biol,* 11**,** R106. https://doi.org/10.1186/gb-2010-11-10-r106

Anders, S., Pyl, P. T. & Huber, W. 2015. HTSeq--a Python framework to work with high-throughput sequencing data. *Bioinformatics,* 31**,** 166-9. https://doi.org/10.1093/bioinformatics/btu638

Annalora, A. J., Marcus, C. B. & Iversen, P. L. 2020. Alternative Splicing in the Nuclear Receptor Superfamily Expands Gene Function to Refine Endo-Xenobiotic Metabolism. *Drug Metab Dispos,* 48**,** 272-287. https://doi.org/10.1124/dmd.119.089102

Bahar Halpern, K., Shenhav, R., Matcovitch-Natan, O., Toth, B., Lemze, D., Golan, M., Massasa, E. E., Baydatch, S., Landen, S., Moor, A. E., Brandis, A., Giladi, A., Stokar-Avihail, A., David, E., Amit, I. & Itzkovitz, S. 2017. Single-cell spatial reconstruction reveals global division of labour in the mammalian liver. *Nature,* 542**,** 352-356. https://doi.org/10.1038/nature21065

Ben-Moshe, S. & Itzkovitz, S. 2019. Spatial heterogeneity in the mammalian liver. *Nat Rev Gastroenterol Hepatol,* 16**,** 395-410. https://doi.org/10.1038/s41575-019-0134-x

Ben-Moshe, S., Shapira, Y., Moor, A. E., Manco, R., Veg, T., Bahar Halpern, K. & Itzkovitz, S. 2019. Spatial sorting enables comprehensive characterization of liver zonation. *Nat Metab,* 1**,** 899-911. https://doi.org/10.1038/s42255-019-0109-9

Benjamini, Y. & Hochberg, Y. 1995. Controlling the False Discovery Rate: A Practical and Powerful Approach to Multiple Testing. *Journal of the Royal Statistical Society: Series B (Methodological),* 57**,** 289-300.

Berrabah, W., Aumercier, P., Lefebvre, P. & Staels, B. 2011. Control of nuclear receptor activities in metabolism by post-translational modifications. *FEBS Lett,* 585**,** 1640-50. https://doi.org/10.1016/j.febslet.2011.03.066

Berthier, A., Johanns, M., Zummo, F. P., Lefebvre, P. & Staels, B. 2021. PPARs in liver physiology. *Biochim Biophys Acta Mol Basis Dis***,** 166097. https://doi.org/10.1016/j.bbadis.2021.166097

Boesjes, M., Bloks, V. W., Hageman, J., Bos, T., Van Dijk, T. H., Havinga, R., Wolters, H., Jonker, J. W., Kuipers, F. & Groen, A. K. 2014. Hepatic farnesoid X-receptor isoforms alpha2 and alpha4 differentially modulate bile salt and lipoprotein metabolism in mice. *PLoS One,* 9**,** e115028. https://doi.org/10.1371/journal.pone.0115028

Bookout, A. L., Jeong, Y., Downes, M., Yu, R. T., Evans, R. M. & Mangelsdorf, D. J. 2006. Anatomical profiling of nuclear receptor expression reveals a hierarchical transcriptional network. *Cell,* 126**,** 789-99. https://doi.org/10.1016/j.cell.2006.06.049

Chaix, A., Deota, S., Bhardwaj, R., Lin, T. & Panda, S. 2021. Sex- and age-dependent outcomes of 9-hour time-restricted feeding of a Western high-fat high-sucrose diet in C57BL/6J mice. *Cell Reports,* 36. https://doi.org/10.1016/j.celrep.2021.109543

Chaix, A., Lin, T., Le, H. D., Chang, M. W. & Panda, S. 2018. Time-Restricted Feeding Prevents Obesity and Metabolic Syndrome in Mice Lacking a Circadian Clock. *Cell Metab*. https://doi.org/10.1016/j.cmet.2018.08.004

Correia, J. C., Massart, J., De Boer, J. F., Porsmyr-Palmertz, M., Martinez-Redondo, V., Agudelo, L. Z., Sinha, I., Meierhofer, D., Ribeiro, V., Bjornholm, M., Sauer, S., Dahlman-Wright, K., Zierath, J. R., Groen, A. K. & Ruas, J. L. 2015. Bioenergetic cues shift FXR splicing towards FXRalpha2 to modulate hepatic lipolysis and fatty acid metabolism. *Mol Metab,* 4**,** 891-902. https://doi.org/10.1016/j.molmet.2015.09.005

Della Torre, S. & Maggi, A. 2017. Sex Differences: A Resultant of an Evolutionary Pressure? *Cell Metab,* 25**,** 499-505. https://doi.org/10.1016/j.cmet.2017.01.006

Deota, S., Lin, T., Chaix, A., Williams, A., Le, H., Calligaro, H., Ramasamy, R., Huang, L. & Panda, S. 2023. Diurnal transcriptome landscape of a multi-tissue response to time-restricted feeding in mammals. *Cell Metab,* 35**,** 150-165 e4. https://doi.org/10.1016/j.cmet.2022.12.006

Dobie, R., Wilson-Kanamori, J. R., Henderson, B. E. P., Smith, J. R., Matchett, K. P., Portman, J. R., Wallenborg, K., Picelli, S., Zagorska, A., Pendem, S. V., Hudson, T. E., Wu, M. M., Budas, G. R., Breckenridge, D. G., Harrison, E. M., Mole, D. J., Wigmore, S. J., Ramachandran, P., Ponting, C. P., Teichmann, S. A., Marioni, J. C. & Henderson, N. C. 2019. Single-Cell Transcriptomics Uncovers Zonation of Function in the Mesenchyme during Liver Fibrosis. *Cell Rep,* 29**,** 1832-1847 e8. https://doi.org/10.1016/j.celrep.2019.10.024

Dobin, A., Davis, C. A., Schlesinger, F., Drenkow, J., Zaleski, C., Jha, S., Batut, P., Chaisson, M. & Gingeras, T. R. 2013. STAR: ultrafast universal RNA-seq aligner. *Bioinformatics,* 29**,** 15-21. https://doi.org/10.1093/bioinformatics/bts635

Droin, C., Kholtei, J. E., Bahar Halpern, K., Hurni, C., Rozenberg, M., Muvkadi, S., Itzkovitz, S. & Naef, F. 2021. Space-time logic of liver gene expression at sub-lobular scale. *Nature Metabolism*. https://doi.org/10.1038/s42255-020-00323-1

Eckel-Mahan, K. L., Patel, V. R., De Mateo, S., Orozco-Solis, R., Ceglia, N. J., Sahar, S., Dilag-Penilla, S. A., Dyar, K. A., Baldi, P. & Sassone-Corsi, P. 2013. Reprogramming of the circadian clock by nutritional challenge. *Cell,* 155**,** 1464-78. https://doi.org/10.1016/j.cell.2013.11.034

Fickert, P., Fuchsbichler, A., Moustafa, T., Wagner, M., Zollner, G., Halilbasic, E., Stoger, U., Arrese, M., Pizarro, M., Solis, N., Carrasco, G., Caligiuri, A., Sombetzki, M., Reisinger, E., Tsybrovskyy, O., Zatloukal, K., Denk, H., Jaeschke, H., Pinzani, M. & Trauner, M. 2009. Farnesoid X receptor critically determines the fibrotic response in mice but is expressed to a low extent in human hepatic stellate cells and periductal myofibroblasts. *Am J Pathol,* 175**,** 2392-405. https://doi.org/10.2353/ajpath.2009.090114

Frevert, U., Engelmann, S., Zougbede, S., Stange, J., Ng, B., Matuschewski, K., Liebes, L. & Yee, H. 2005. Intravital observation of Plasmodium berghei sporozoite infection of the liver. *PLoS Biol,* 3**,** e192. https://doi.org/10.1371/journal.pbio.0030192

Garrido, A., Kim, E., Teijeiro, A., Sanchez, P. S., Gallo, R., Nair, A., Matamala Montoya, M., Perna, C., Vicent, G. P., Munoz, J., Campos-Olivas, R., Melms, J. C., Izar, B., Schwabe, R. F. & Djouder, N. 2021. Histone acetylation of bile acid transporter genes plays a critical role in cirrhosis. *J Hepatol*. https://doi.org/10.1016/j.jhep.2021.12.019

Gonzalez-Sanchez, E., Firrincieli, D., Housset, C. & Chignard, N. 2017. Expression patterns of nuclear receptors in parenchymal and non-parenchymal mouse liver cells and their modulation in cholestasis. *Biochim Biophys Acta Mol Basis Dis,* 1863**,** 1699-1708. https://doi.org/10.1016/j.bbadis.2017.04.004

Guille, L., Johanns, M., Zummo, F.-P., Staels, B., Lefebvre, P., Eeckhoute, J. & Dubois-Chevalier, J. 2022. ISCEBERG : Interactive Single Cell Expression Browser for Exploration of RNAseq data using Graphics (v1.0.1). Zenodo, doi:10.5281/zenodo.6563734

Halpern, K. B., Shenhav, R., Massalha, H., Toth, B., Egozi, A., Massasa, E. E., Medgalia, C., David, E., Giladi, A., Moor, A. E., Porat, Z., Amit, I. & Itzkovitz, S. 2018. Paired-cell sequencing enables spatial gene expression mapping of liver endothelial cells. *Nat Biotechnol,* 36**,** 962-970. https://doi.org/10.1038/nbt.4231

Hatori, M., Vollmers, C., Zarrinpar, A., Ditacchio, L., Bushong, E. A., Gill, S., Leblanc, M., Chaix, A., Joens, M., Fitzpatrick, J. A., Ellisman, M. H. & Panda, S. 2012. Time-restricted feeding without reducing caloric intake prevents metabolic diseases in mice fed a high-fat diet. *Cell Metab,* 15**,** 848-60. https://doi.org/10.1016/j.cmet.2012.04.019

Hu, Y., Zhan, Q., Liu, H. X., Chau, T., Li, Y. & Wan, Y. J. 2014. Accelerated partial hepatectomy-induced liver cell proliferation is associated with liver injury in Nur77 knockout mice. *Am J Pathol,* 184**,** 3272-83. https://doi.org/10.1016/j.ajpath.2014.08.002

Hughes, M. E., Hogenesch, J. B. & Kornacker, K. 2010. JTK_CYCLE: an efficient nonparametric algorithm for detecting rhythmic components in genome-scale data sets. *J Biol Rhythms,* 25**,** 372-80. https://doi.org/10.1177/0748730410379711

Katz, Y., Wang, E. T., Silterra, J., Schwartz, S., Wong, B., Thorvaldsdottir, H., Robinson, J. T., Mesirov, J. P., Airoldi, E. M. & Burge, C. B. 2015. Quantitative visualization of alternative exon expression from RNA-seq data. *Bioinformatics,* 31**,** 2400-2. https://doi.org/10.1093/bioinformatics/btv034

Kechin, A., Boyarskikh, U., Kel, A. & Filipenko, M. 2017. cutPrimers: A New Tool for Accurate Cutting of Primers from Reads of Targeted Next Generation Sequencing. *J Comput Biol,* 24**,** 1138-1143. https://doi.org/10.1089/cmb.2017.0096

Kietzmann, T. 2017. Metabolic zonation of the liver: The oxygen gradient revisited. *Redox Biol,* 11**,** 622-630. https://doi.org/10.1016/j.redox.2017.01.012

Lefebvre, B., Benomar, Y., Guedin, A., Langlois, A., Hennuyer, N., Dumont, J., Bouchaert, E., Dacquet, C., Penicaud, L., Casteilla, L., Pattou, F., Ktorza, A., Staels, B. & Lefebvre, P. 2010. Proteasomal degradation of retinoid X receptor alpha reprograms transcriptional activity of PPARgamma in obese mice and humans. *J Clin Invest,* 120**,** 1454-68. https://doi.org/10.1172/JCI38606

Li, Z., Kruijt, J. K., Van Der Sluis, R. J., Van Berkel, T. J. & Hoekstra, M. 2013. Nuclear receptor atlas of female mouse liver parenchymal, endothelial, and Kupffer cells. *Physiol Genomics,* 45**,** 268-75. https://doi.org/10.1152/physiolgenomics.00151.2012

Love, M. I., Huber, W. & Anders, S. 2014. Moderated estimation of fold change and dispersion for RNA-seq data with DESeq2. *Genome Biol,* 15**,** 550. https://doi.org/10.1186/s13059-014-0550-8

Lu, Y. F., Jin, T., Xu, Y., Zhang, D., Wu, Q., Zhang, Y. K. & Liu, J. 2013. Sex differences in the circadian variation of cytochrome p450 genes and corresponding nuclear receptors in mouse liver. *Chronobiol Int,* 30**,** 1135-43. https://doi.org/10.3109/07420528.2013.805762

Mederacke, I., Dapito, D. H., Affo, S., Uchinami, H. & Schwabe, R. F. 2015. High-yield and high-purity isolation of hepatic stellate cells from normal and fibrotic mouse livers. *Nat Protoc,* 10**,** 305-15. https://doi.org/10.1038/nprot.2015.017

Mukha, A., Kalkhoven, E. & Van Mil, S. W. C. 2021. Splice variants of metabolic nuclear receptors: Relevance for metabolic disease and therapeutic targeting. *Biochim Biophys Acta Mol Basis Dis,* 1867**,** 166183. https://doi.org/10.1016/j.bbadis.2021.166183

Nagy, P., Thorgeirsson, S. S. & Grisham, J. W. 2020. Organizational Principles of the Liver. *The Liver.*

Natale, D. A., Arighi, C. N., Blake, J. A., Bona, J., Chen, C., Chen, S. C., Christie, K. R., Cowart, J., D'eustachio, P., Diehl, A. D., Drabkin, H. J., Duncan, W. D., Huang, H., Ren, J., Ross, K., Ruttenberg, A., Shamovsky, V., Smith, B., Wang, Q., Zhang, J., El-Sayed, A. & Wu, C. H. 2017. Protein Ontology (PRO): enhancing and scaling up the representation of protein entities. *Nucleic Acids Res,* 45**,** D339-D346. https://doi.org/10.1093/nar/gkw1075

Nishimura, M., Naito, S. & Yokoi, T. 2004. Tissue-specific mRNA expression profiles of human nuclear receptor subfamilies. *Drug Metab Pharmacokinet,* 19**,** 135-49. https://doi.org/10.2133/dmpk.19.135

Panday, R., Monckton, C. P. & Khetani, S. R. 2022. The Role of Liver Zonation in Physiology, Regeneration, and Disease. *Semin Liver Dis,* 42**,** 1-16. https://doi.org/10.1055/s-0041-1742279

Payen, V. L., Lavergne, A., Alevra Sarika, N., Colonval, M., Karim, L., Deckers, M., Najimi, M., Coppieters, W., Charloteaux, B., Sokal, E. M. & El Taghdouini, A. 2021. Single-cell RNA sequencing of human liver reveals hepatic stellate cell heterogeneity. *JHEP Rep,* 3**,** 100278. https://doi.org/10.1016/j.jhepr.2021.100278

Pei, L., Waki, H., Vaitheesvaran, B., Wilpitz, D. C., Kurland, I. J. & Tontonoz, P. 2006. NR4A orphan nuclear receptors are transcriptional regulators of hepatic glucose metabolism. *Nat Med,* 12**,** 1048-55. https://doi.org/10.1038/nm1471

Pols, T. W., Ottenhoff, R., Vos, M., Levels, J. H., Quax, P. H., Meijers, J. C., Pannekoek, H., Groen, A. K. & De Vries, C. J. 2008. Nur77 modulates hepatic lipid metabolism through suppression of SREBP1c activity. *Biochem. Biophys. Res. Commun,* 366**,** 910-916.

Praestholm, S. M., Correia, C. M. & Grontved, L. 2020. Multifaceted Control of GR Signaling and Its Impact on Hepatic Transcriptional Networks and Metabolism. *Front Endocrinol (Lausanne),* 11**,** 572981. https://doi.org/10.3389/fendo.2020.572981

Ramos Pittol, J. M., Milona, A., Morris, I., Willemsen, E. C. L., Van Der Veen, S. W., Kalkhoven, E. & Van Mil, S. W. C. 2020. FXR Isoforms Control Different Metabolic Functions in Liver Cells via Binding to Specific DNA Motifs. *Gastroenterology*. https://doi.org/10.1053/j.gastro.2020.07.036

Ritchie, M. E., Phipson, B., Wu, D., Hu, Y., Law, C. W., Shi, W. & Smyth, G. K. 2015. limma powers differential expression analyses for RNA-sequencing and microarray studies. *Nucleic Acids Res,* 43**,** e47. https://doi.org/10.1093/nar/gkv007

Robinson, J. T., Thorvaldsdottir, H., Winckler, W., Guttman, M., Lander, E. S., Getz, G. & Mesirov, J. P. 2011. Integrative genomics viewer. *Nat. Biotechnol,* 29**,** 24-26.

Schmittgen, T. D. & Livak, K. J. 2008. Analyzing real-time PCR data by the comparative CT method. *Nature Protocols,* 3**,** 1101-1108. https://doi.org/10.1038/nprot.2008.73

Soccio, R. E. 2020. Hepatic Nuclear Receptors. *The Liver.*

Su, T., Yang, Y., Lai, S., Jeong, J., Jung, Y., Mcconnell, M., Utsumi, T. & Iwakiri, Y. 2021. Single-Cell Transcriptomics Reveals Zone-Specific Alterations of Liver Sinusoidal Endothelial Cells in Cirrhosis. *Cell Mol Gastroenterol Hepatol,* 11**,** 1139-1161. https://doi.org/10.1016/j.jcmgh.2020.12.007

Uniprot, C. 2021. UniProt: the universal protein knowledgebase in 2021. *Nucleic Acids Res,* 49**,** D480-D489. https://doi.org/10.1093/nar/gkaa1100

Vandel, J., Gheeraert, C., Staels, B., Eeckhoute, J., Lefebvre, P. & Dubois-Chevalier, J. 2020. GIANT: galaxy-based tool for interactive analysis of transcriptomic data. *Scientific Reports,* 10. https://doi.org/10.1038/s41598-020-76769-w

Vaquero, J., Monte, M. J., Dominguez, M., Muntane, J. & Marin, J. J. 2013. Differential activation of the human farnesoid X receptor depends on the pattern of expressed isoforms and the bile acid pool composition. *Biochem Pharmacol,* 86**,** 926-39. https://doi.org/10.1016/j.bcp.2013.07.022

Verbeke, L., Farre, R., Trebicka, J., Komuta, M., Roskams, T., Klein, S., Elst, I. V., Windmolders, P., Vanuytsel, T., Nevens, F. & Laleman, W. 2014. Obeticholic acid, a farnesoid X receptor agonist, improves portal hypertension by two distinct pathways in cirrhotic rats. *Hepatology,* 59**,** 2286-98. https://doi.org/10.1002/hep.26939

Vollmers, C., Gill, S., Ditacchio, L., Pulivarthy, S. R., Le, H. D. & Panda, S. 2009. Time of feeding and the intrinsic circadian clock drive rhythms in hepatic gene expression. *Proc Natl Acad Sci U S A,* 106**,** 21453-8. https://doi.org/10.1073/pnas.0909591106

Weikum, E. R., Liu, X. & Ortlund, E. A. 2018. The nuclear receptor superfamily: A structural perspective. *Protein Sci,* 27**,** 1876-1892. https://doi.org/10.1002/pro.3496

FIGURE LEGENDS

Figure 1 – Liver cell type isolation protocol. The sequential steps of liver cell type purification by fluorescence-activated cell sorting (FACS) are shown here. A) Hepatocyte purification; B) non-parenchymal cells isolation. Assessed parameters by FACS were: viability: Zombie green-negative; HCs: sorted based on size; HSCs: UV-positive; LSECs: CD45-negative, CD31-positive, CD146-positive; KCs: CD45-positive, Clec4F-positive, F4/80-positive; CHs: CD45-positive, CD31-negative, CD146-negative, CD326-positive. Details of the complete procedure can be found in the Material & Methods section. HCs: hepatocytes; NPC: nonparenchymal cells; KCs Kupffer cells; CHs: cholangiocytes; LSECs: liver sinusoidal endothelial cells; HSCs: hepatic stellate cells. An example of the FACS output is shown in Supplemental Figure 1.

Figure 2. Characterization of purified liver cell types. After FACS-based purification, RNA was extracted and used for RT-qPCR assays (left panels) or cells were deposited on a glass slide using Cytospin centrifugation to be further labelled with the indicated antibodies. A) HCs characterization; B) HSCs characterization; C) KCs characterization; D) LSECs characterization; E) CHs characterization.

Figure 3. Circadian expression of nuclear receptors. Mice were fed a chow diet either ad libitum or under a time-restricted regimen for 2 weeks. Liver were collected at indicated times (ZT0 being “lights-on) and extracted RNAs were analyzed on Affymetrix arrays (n=3). Data were processed and gene expression values for NRs were extracted and used to generate a heatmap. AdLib and TRF transcriptomic data were also analyzed using the JTK_cycle R script to identify genes displaying a cyclic expression with a ≈24-hour period. C: Cyclically-expressed genes, NC: non-cyclically expressed genes.

Figure 4. NR expression in purified liver cell types. RNA extracted from each cell type preparation (n=3) was analyzed by single-end 50b RNAseq. After (pre)processing, mapping and normalization by the median-of-ratios method to make counts comparable between samples, $\log_2$ expression values were used to generate a bubble plot in which row Z-score of RPKM ($p\ adj < 0.05$) is indicated (genes in red are up-regulated, genes in blue are down-regulated) on a row-by-row basis. The size of the bubble is proportional to the expression level (empty spaces indicate no significant expression).

Figure 5. NR isoforms expression in purified liver cell types. Gene expression data were reported from Figure 4 and Uniprot-identified isoforms were indicated. Non-detected isoforms are indicated in gray. (Co)Identified corresponding transcripts are indicated for each cell type and NR.

Figure 6. NR zonation in hepatocytes. Upper panel: Schematic organization of a liver trabeculae [(adapted from Wikimedia Commons and initially published in (Frevert et al., 2005)]. Lower panel: expression values for each NR were extracted from (Bahar Halpern et al., 2017) and used to compute an heatmap. Only NRs displaying variable expression along the periportal-pericentral axis are shown. Red: High expression, white: low expression. Note that gene expression levels are indicated for a single transcript along the pericentral to periportal axis. Arrow (right to left) indicates the bile flow, arrows (left to right) indicate the blood flow.

Supplemental Figure 1. Gating strategy for liver cell type isolation. An illustration of the flow cytometric analysis/sorting is shown here (NPC25). Cells were selected as non-debris on FSC/SSC scatters and singlets were gated on FSC-H/FSC-W. Live cells were selected as "low" for Zombie Green staining. The polychromatic flow cytometry strategy was applied to isolate indicated liver cell types. Further details can be found in the Material & Methods section as well as in Figure 1.

Supplemental Figure 2. Numbering of purified cells. Cell numbers obtained after the FACS procedure are indicated (n=5-14). KCs Kupffer cells; CHs: cholangiocytes; LSECs: liver sinusoidal endothelial cells; HSCs: hepatic stellate cells.

Supplemental Figure 3. Cell purity assessment by gene expression profiling. RNAs extracted from each purified cell type was analyzed by RT-qPCR (n=9-16) and probed for the expression of ubiquitous (*Rplp0*/*36b4*), common (HCs and CHs, *Ck18*) or specific (HSCs: *Dcn*, *Acta2*, *Des*; CHs: *Sox9*, *Epcam*, *Sglt1*, *Prom1*, *Jag1*; KCs: *Cd68*; LSECs: *Cdh5*) cell markers.

Supplemental Figure 4. NR zonation in liver sinusoidal endothelial cells. Upper panel: Schematic organization of a liver trabeculae [adapted from Wikimedia Commons and initially published in (Frevert et al., 2005)]. Lower panel: expression values for each NR were extracted from (Halpern et al., 2018) and used to compute an heatmap. Note that gene expression levels are indicated for a single transcript

along the pericentral to periportal axis. Red: High expression, white: low expression. Arrow (right to left) indicates the bile flow, arrows (left to right) indicate the blood flow.

Supplemental Figure 5. NR zonation in liver sinusoidal endothelial cells. Upper panel: Schematic organization of a liver trabeculae [adapted from Wikimedia Commons and initially published in (Frevert et al., 2005)]. Lower panel: expression values for each NR were extracted from (Su et al., 2021) and used to compute an heatmap. Note that gene expression levels are indicated for a single transcript along the pericentral to periportal axis. Red: High expression, white: low expression. Arrow (right to left) indicates the bile flow, arrows (left to right) indicate the blood flow.

Supplemental Figure 6. NR zonation in hepatic stellate cells. Upper panel: Schematic organization of a liver trabeculae [adapted from Wikimedia Commons and initially published in (Frevert et al., 2005)]. Lower panel: expression values for each NR were extracted from (Dobie et al., 2019) and used to generate a bubble plot in which the color gradient indicates the expression level (blue: low expression, red: high expression) and the circle diameter indicates the number of cells expressing the transcript. Arrow (right to left) indicates the bile flow, arrows (left to right) indicate the blood flow.

Supplemental Table 1. List of primers used in RT-qPCR experiments.

Supplemental Table 2. JTK_cycle output. Time-dependent transcriptomic data were analyzed using the JTK_cycle R script. Sheet 1: JTK_cycle output for whole liver from ad libitum-fed (AdLib) mice. Sheet 2: JTK_cycle output for whole liver from time-restricted-fed (TRF) mice.

Supplemental Table 3. NR gene counts and NR isoform description. Sheet 1: Normalized average (n=3) RPKMs are indicated for each mouse NR. The color scale compares NR expression level between cell types (from white, no expression to red, highest expression), numbers are the averaged RPKM.

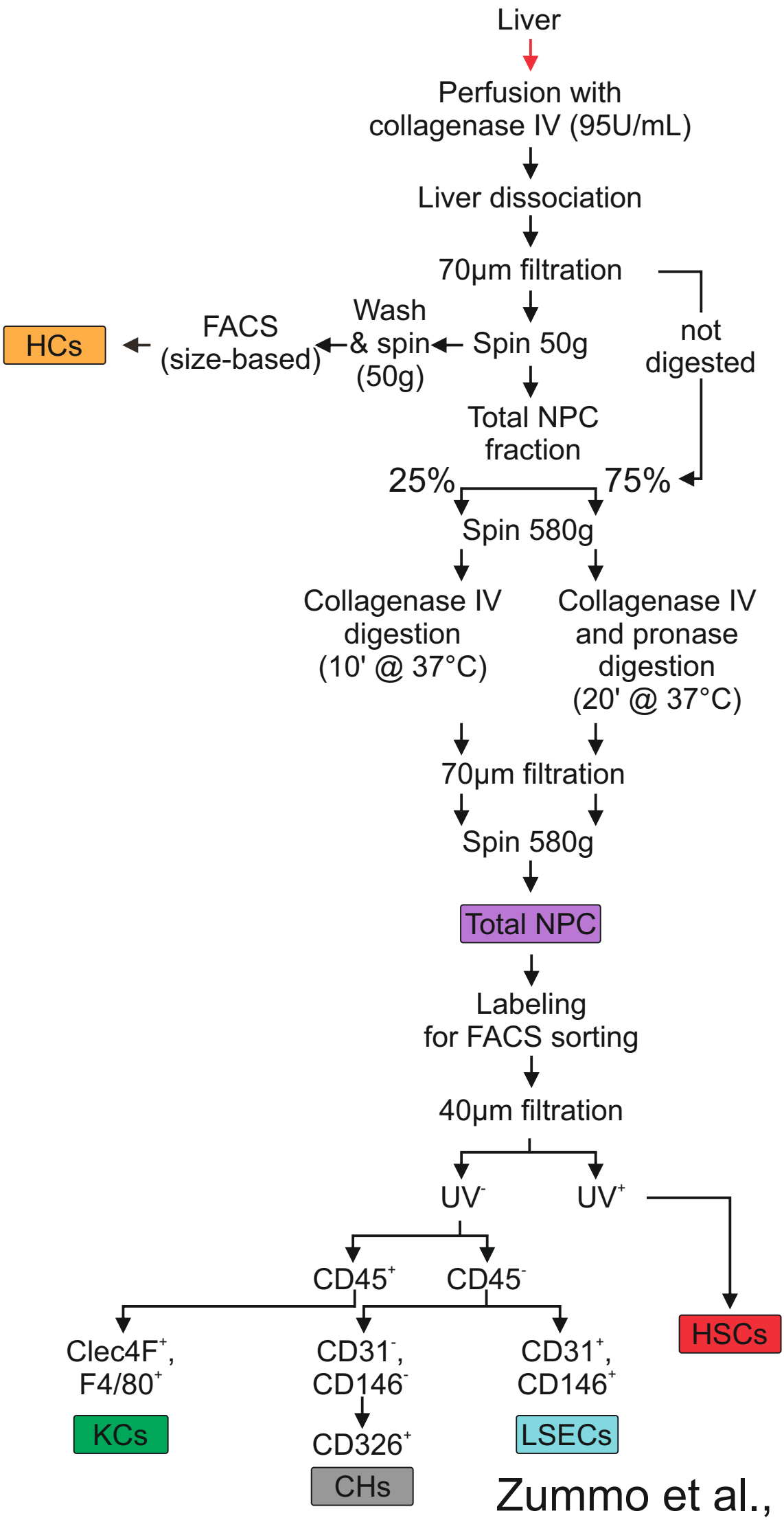

Zummo et al., Figure 1

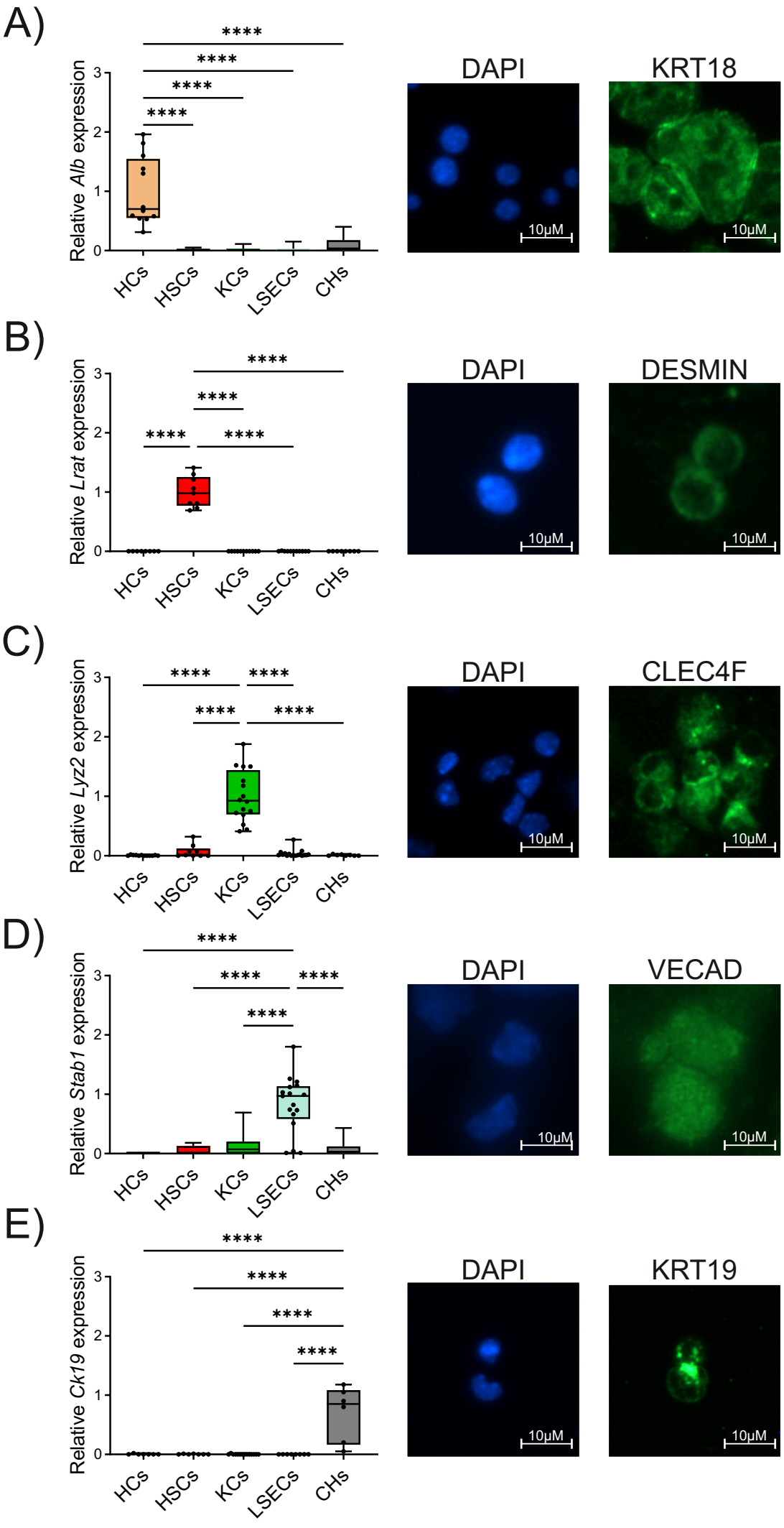

Zummo et al., Figure 2

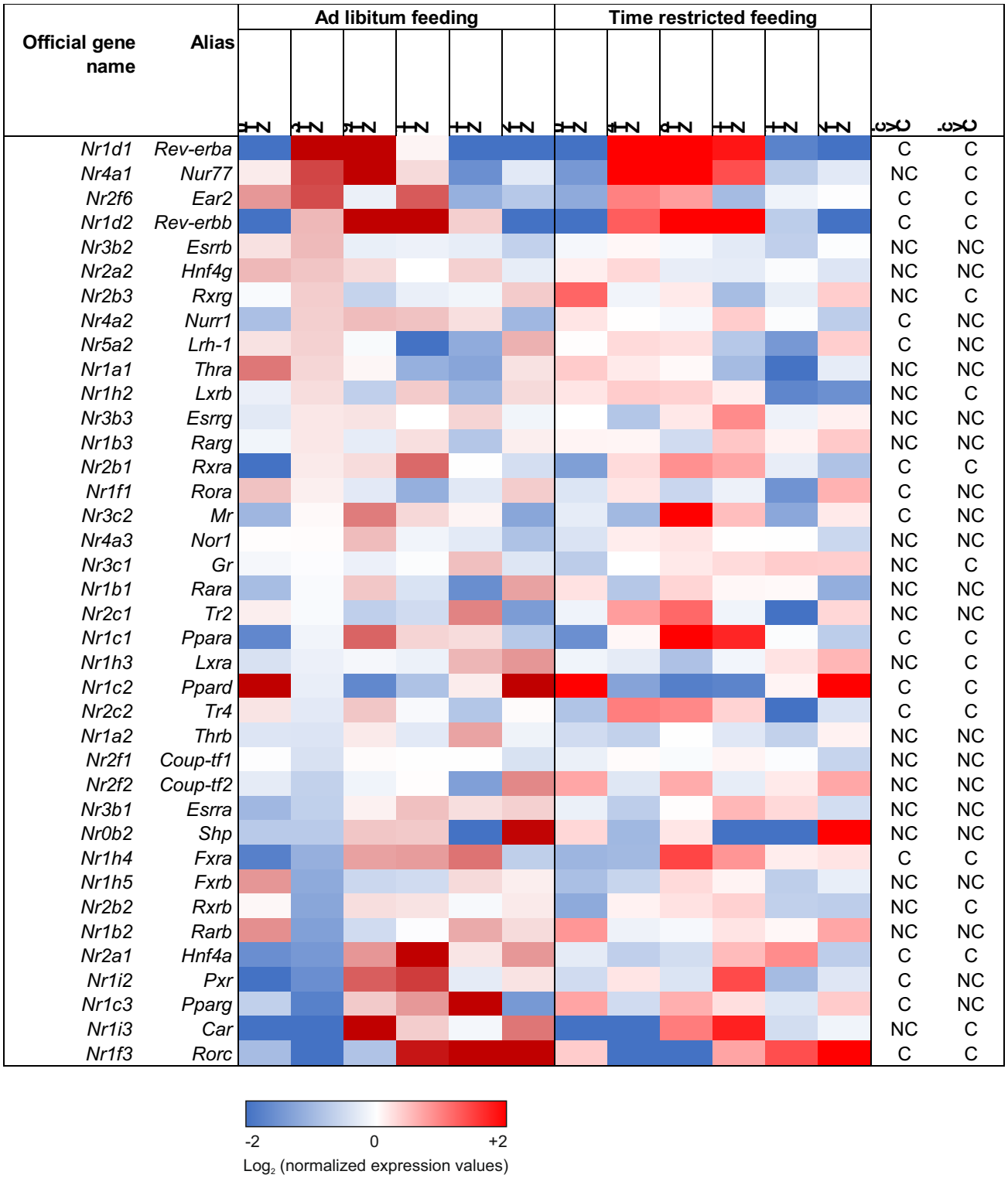

Zummo et al., Figure 3

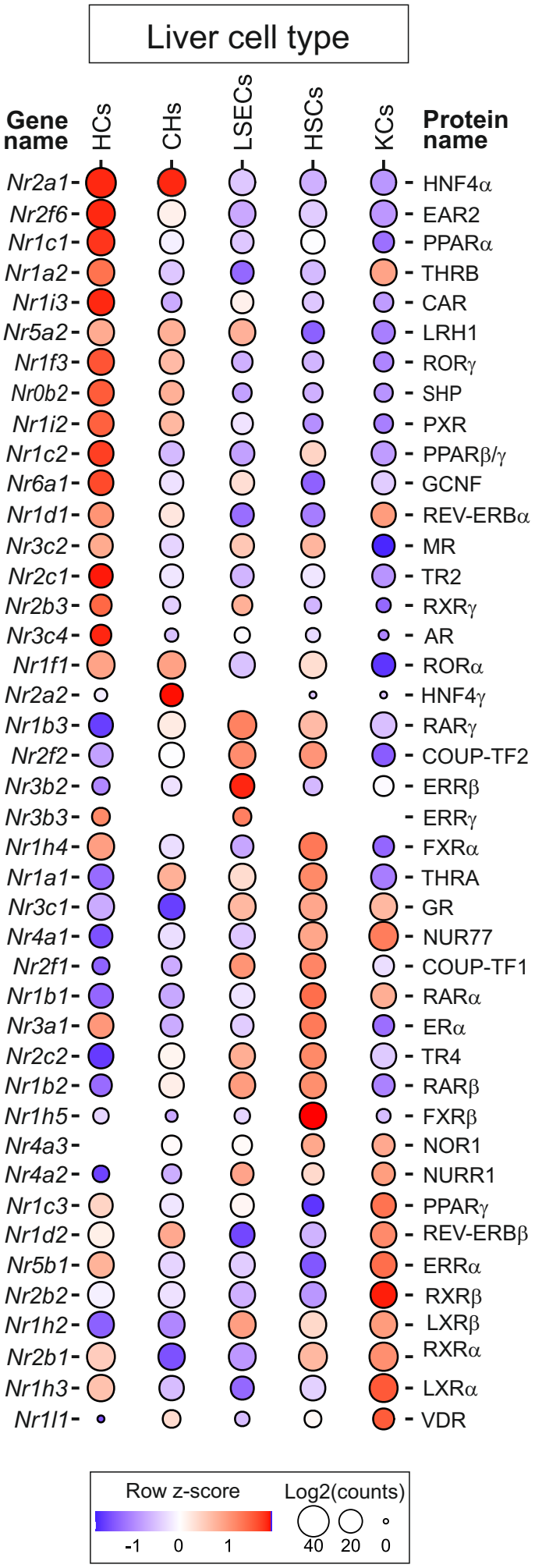

Zummo et al., Figure 4

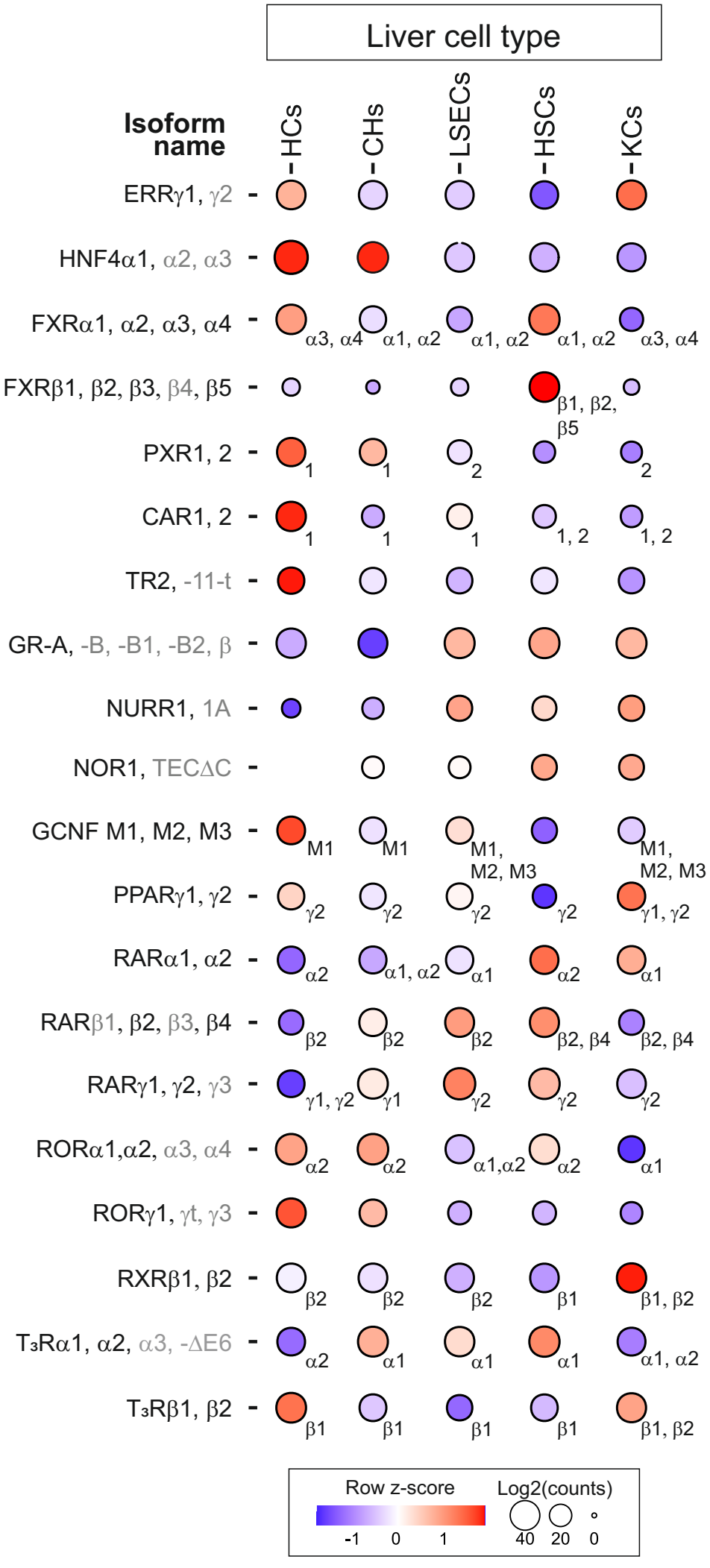

Zummo et al., Figure 5

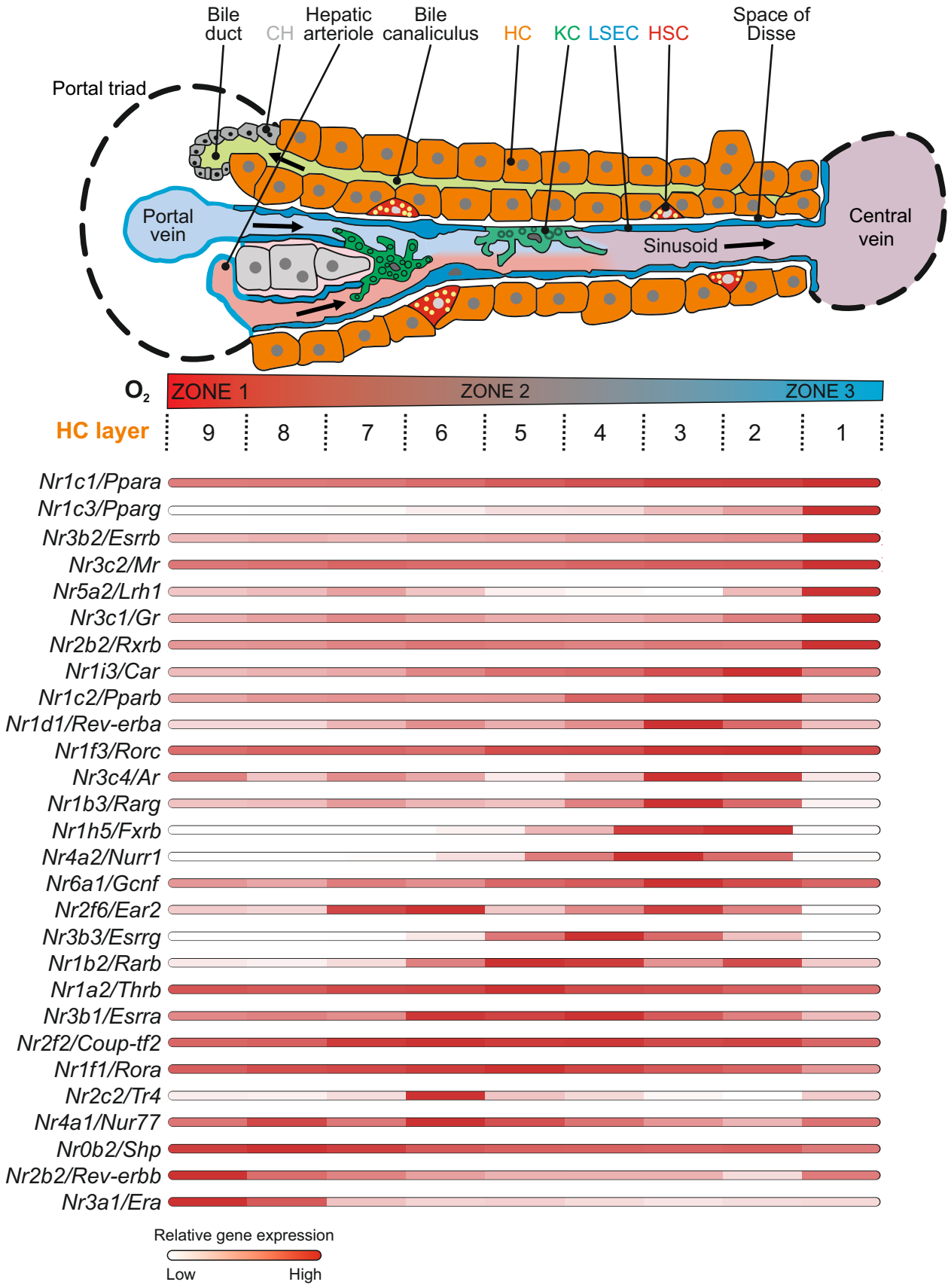

Zummo et al., Figure 6

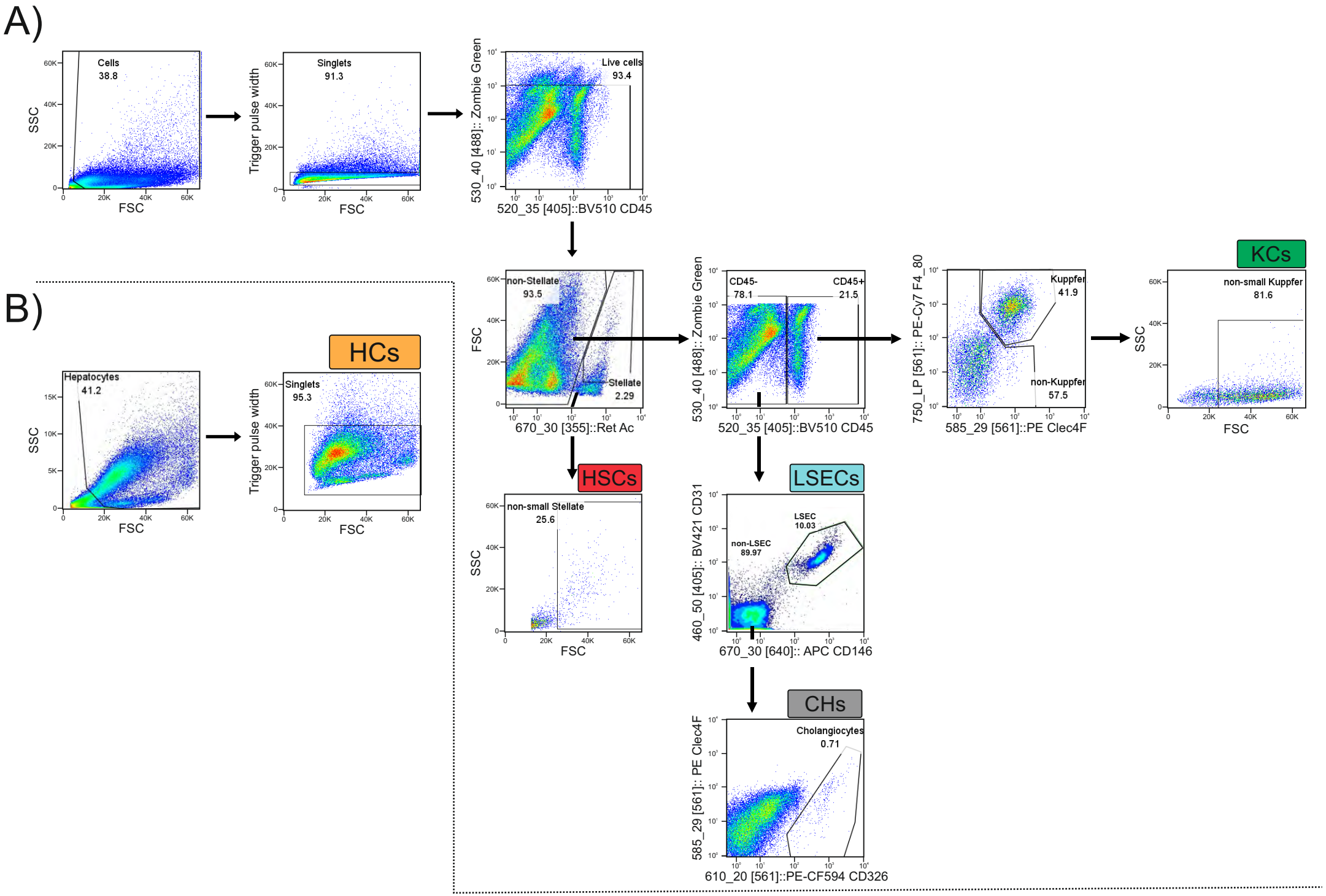

Zummo et al., Supp. Figure 1

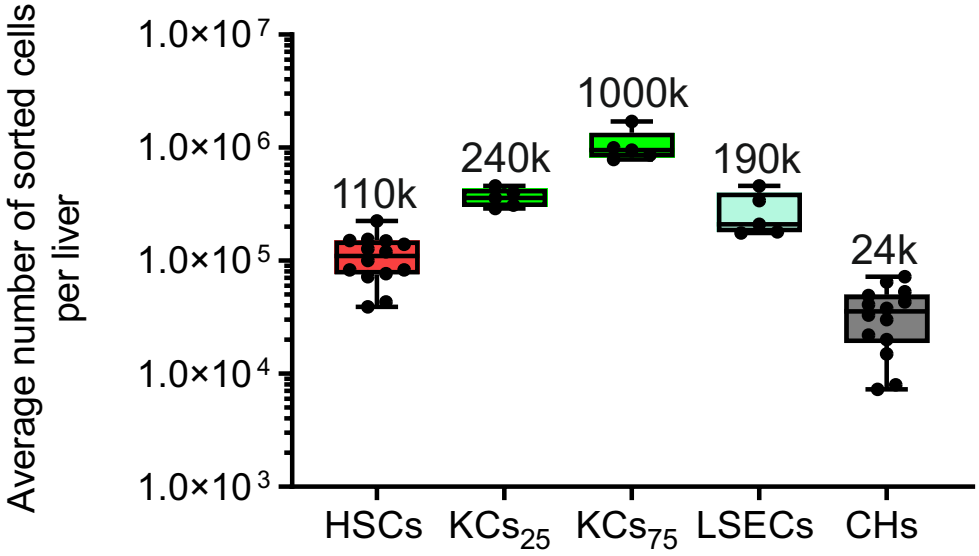

Zummo et al., Supp. Figure 2

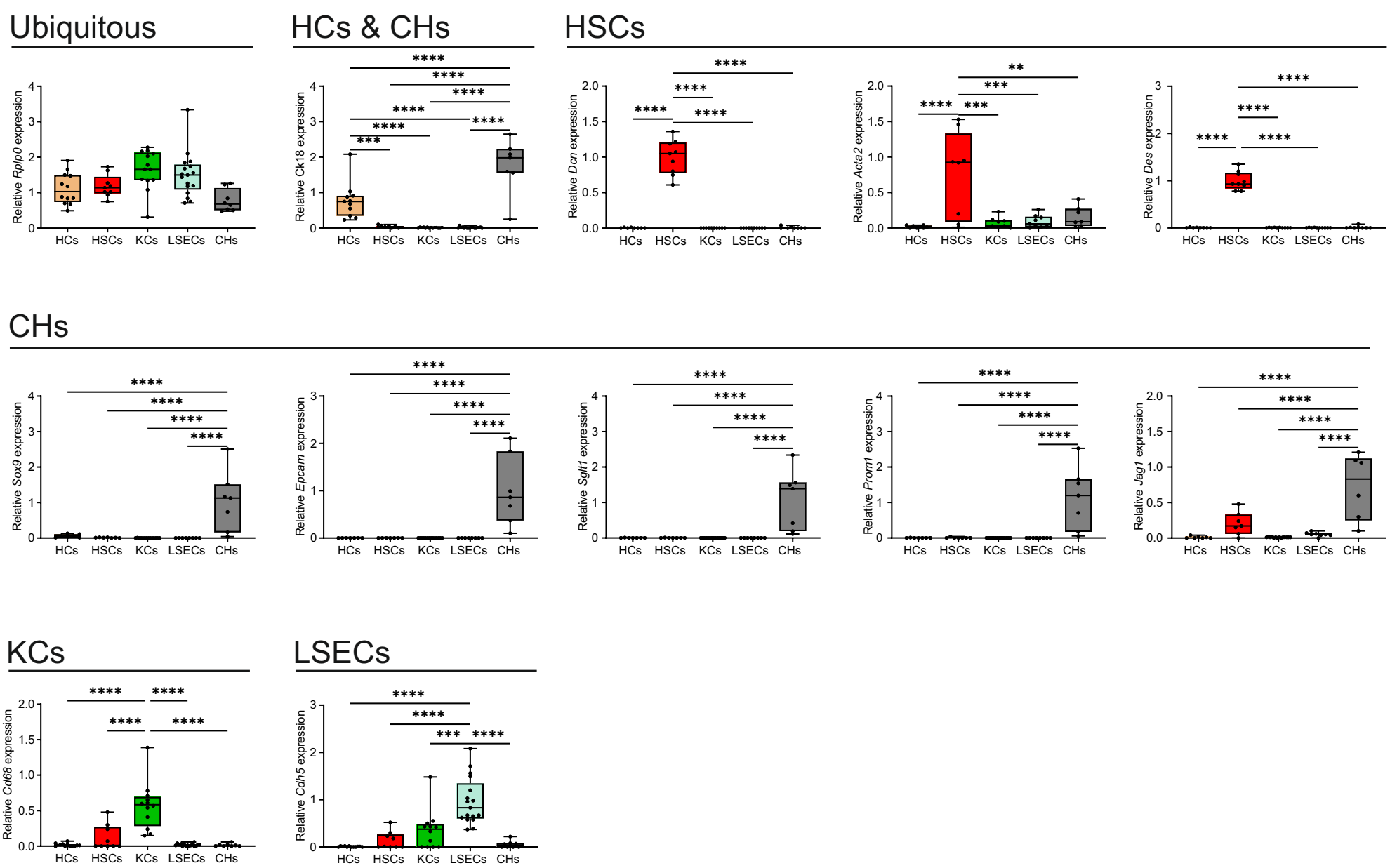

Zummo et al., Supp. Figure 3

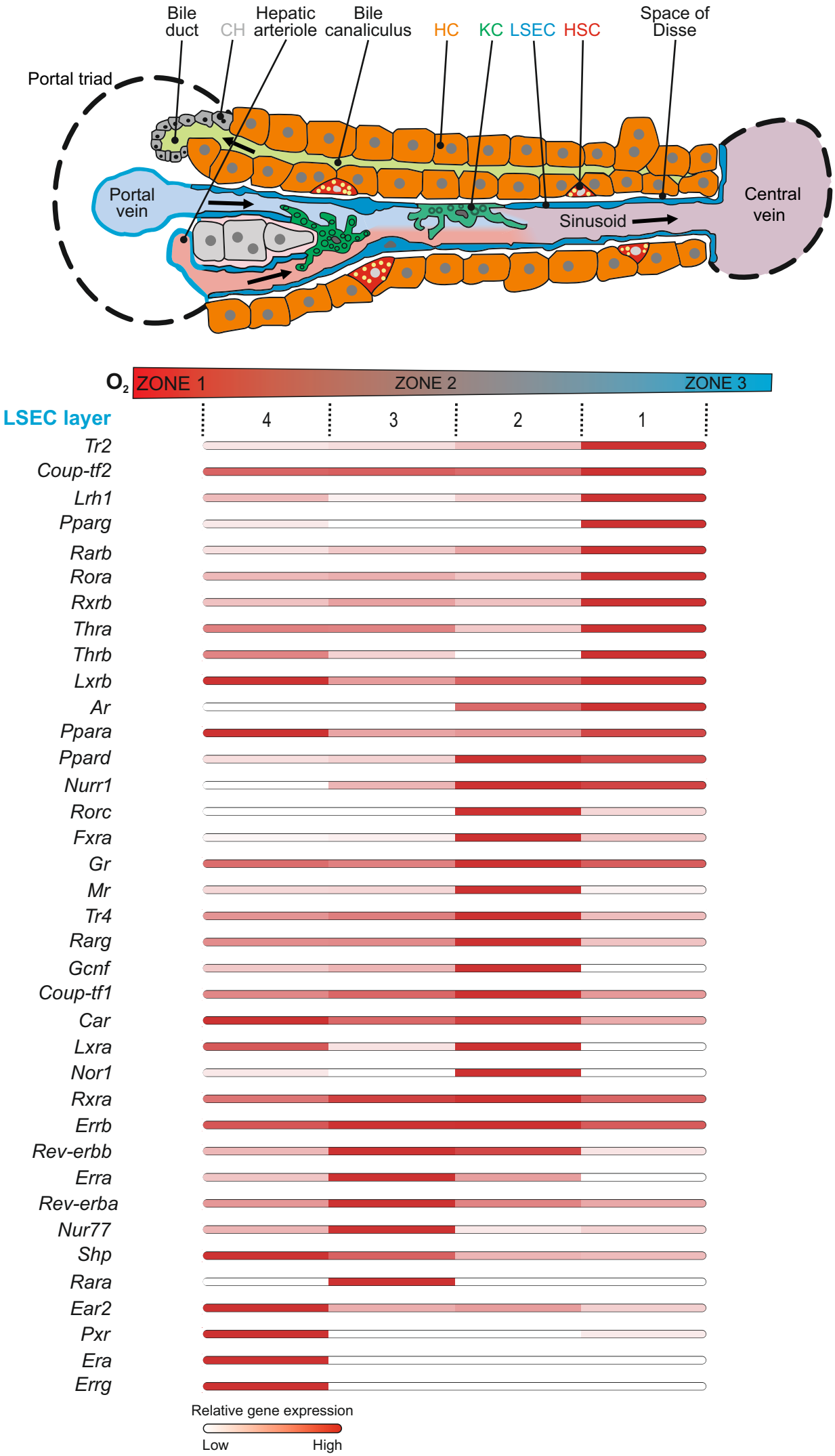

Zummo et al., Supp. Figure 4

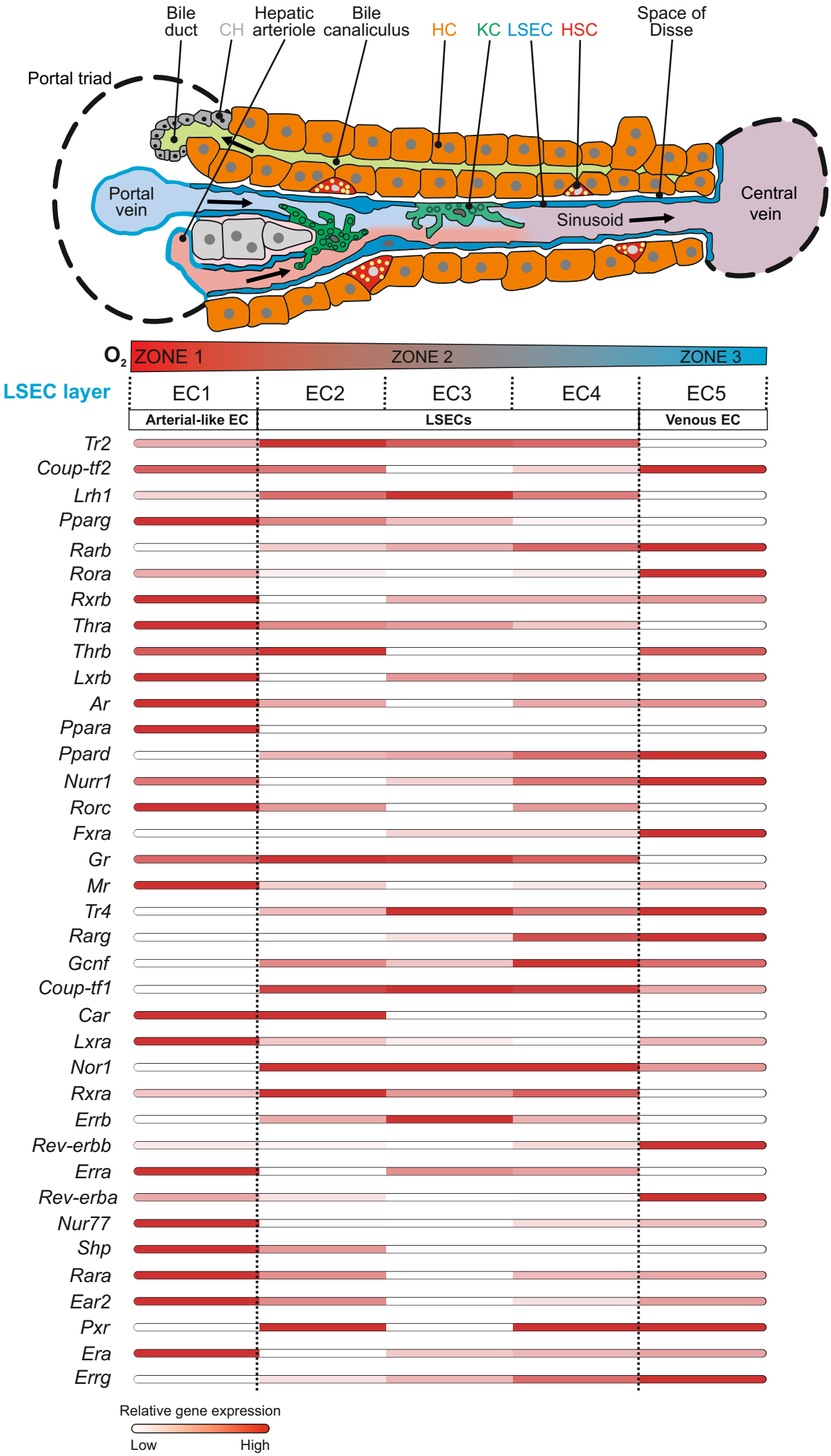

Zummo et al., Supp. Figure 5

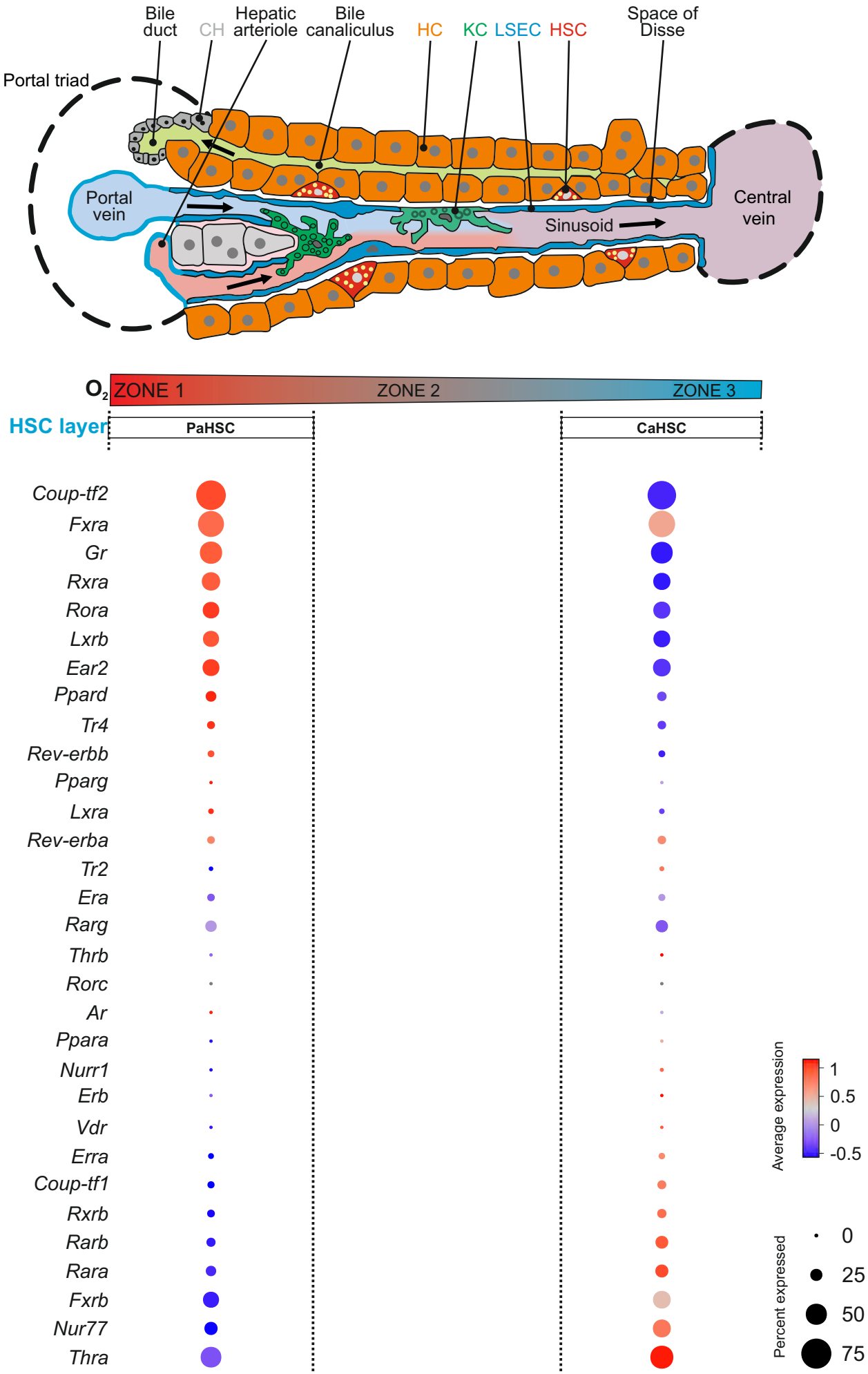

Zummo et al., Supp. Figure 6